Flow Rate Independent Multiscale Liquid Biopsy for Precision Oncology

Jing Yan[*1], Jie Wang[2], Robert Dallmann[3], Renquan Lu[4], and Jérôme Charmet*[*3,5]*

1 Holosensor Medical Technology Ltd., Suzhou, 215000, China,
2 Institute for Advanced Materials, School of Material Science and Engineering, Jiangsu University, Zhenjiang 212013, China,
3 Division of Biomedical Sciences, Warwick Medical School, University of Warwick, Coventry CV4 7AL, United Kingdom,
4 Department of Clinical Laboratory, Fudan University Shanghai Cancer Center, Shanghai, 200032, China,
5 School of Engineering – HE-Arc Ingénierie, HES-SO University of Applied Sciences Western Switzerland, 2000 Neuchâtel, Switzerland.

Abstract

Immunoaffinity-based liquid biopsies of circulating tumour cells (CTCs) hold great promise for cancer management, but typically suffer from low throughput, relative complexity and post-processing limitations. Here we address these issues simultaneously by decoupling and independently optimising the nano-, micro- and macro-scales of a CTC enrichment device that is both simple to fabricate and operate. At its core is a scalable macroscale mesh with optimised micropores, nano-functionalised with antibodies against cell surface proteins. Unlike other affinity-based liquid biopsies, optimum capture can be achieved independently of the flow rate, as demonstrated with constant capture efficiencies, above 75%, between 50–200 µL min^{-1}. The device achieved 96% sensitivity and 100% specificity when used to detect CTCs in the blood of 79 cancer patients and 20 healthy controls. To demonstrate its post-processing capabilities, we used immunofluorescence labelling to identify PD-L1+ CTCs in 36% of patients (n=33) as potential responders to immune checkpoint inhibition therapy. Finally, our device achieved an 80% positive match in the identification of HER2+ breast cancer (n=26) compared to clinical standard FISH on solid biopsy. The results suggest that our approach, which overcomes major limitations previously associated with affinity-based liquid biopsies, could provide a versatile tool to improve cancer management.

** corresponding authors*

Introduction

Liquid biopsies have the potential to transform cancer management through non-invasive, real-time feedback on patient conditions[1–4]. Circulating tumor cells (CTCs) that are released from primary and/or distant tumours into the bloodstream[5], are seen as a particularly useful source of information to improve clinical outcome (patient prognosis, real-time responses to therapeutic interventions, monitoring of tumour recurrence), guide drug discovery, and advance our understanding of cancer progression, metastatic cascade, and minimal residual diseases [6–9]. However, the capture of such cells from blood is technically challenging due to their low abundance, typically 1-10 CTCs per mL [10–12]. This constraint imposes the processing of a large sample volume, usually between 4-10 mL, to retrieve enough cells. Consequently, the ideal device must combine high capture efficiency and high throughput.

Surface based capture strategies, using e.g., antibodies to bind CTC-specific surface marker proteins, typically suffer from low throughput [3,13]. This is because optimal mass transfer of the target cells to the functionalised surface typically requires short diffusion distance and low fluid velocity to enhance the probability of receptor-ligand interaction. The low fluid velocity will also minimise the cells' exposure to shear stress after capture, which is desirable[11,14]. Short diffusion distances are typically encountered in microfluidic devices, which explains their pivotal role in the field and enables size-independent, high efficiency capture of bioparticles [2,3,10,13–15]. However, low fluid velocity in microfluidic devices typically puts an upper limit on the flow rate, thereby constraining the throughput of the assay. Indeed, most affinity based microfluidic devices proposed to date have an upper limit of a few mL h^{-1}, above which the capture efficiency drops significantly (typically up to 2 mL h^{-1} as reported in a number of reviews [3,11,17,18]). In addition to the flow rate limitation, affinity-based liquid biopsy devices are typically complex due to their inherent small sizes and channel geometries (e.g., [18–20]). Finally, such devices do not always allow for easy post-processing since the cells are typically surface-bound inside the chip and not easily accessible or retrievable.

Here we present a novel and simple strategy that addresses all three issues (flow rate, complexity and limited post processing capability) at the same time. First, flow rate independent capture is achieved by decoupling and independently optimising the three characteristic length scales of the device, which is not possible in conventional microfluidic devices. Our device consists of 1) a macroscale channel that allows high flow rate processing while maintaining low fluid velocity, 2) a microscale mesh that promotes optimal interaction with the target cells and 3) a nano-functionalised surface, which enables high capture efficiency and low non-specific interaction (Fig. 1a-d). The target cells are captured on the mesh via interaction between surface markers and complementary antibodies tethered to the nano-functionalised surface, while the non-targeted cells flow through unaffected. Our device can be conceptualised as an array of (thousands of) parallel microchannels, optimised for liquid biopsy (Fig. 1a). The advantage of our approach is that the scaling of the macroscale dimension does not compromise the micro- or nano-scale properties. Thus, we demonstrate an optimised capture efficiency above 75% for flow rates as high as 200 µL min^{-1} (or 12 mL h^{-1}), which is approximately an order of magnitude higher than most commonly reported values for surface-based capture in conventional microfluidic devices[11,17,19–21]. We validate the device clinically by isolating CTCs in 4 mL blood samples from 79 cancer patients. The sensitivity and specificity of our device using conventional staining protocols to identify the CTCs were of 96% and 100%, respectively.

Second, the production of our simple device does not rely on complex microfabrication processes. Its operation only requires an external pumping system to apply negative pressure (Fig. 1e-i) to process manually loaded buffers and samples (the detailed process steps are shown in Fig. SM1).

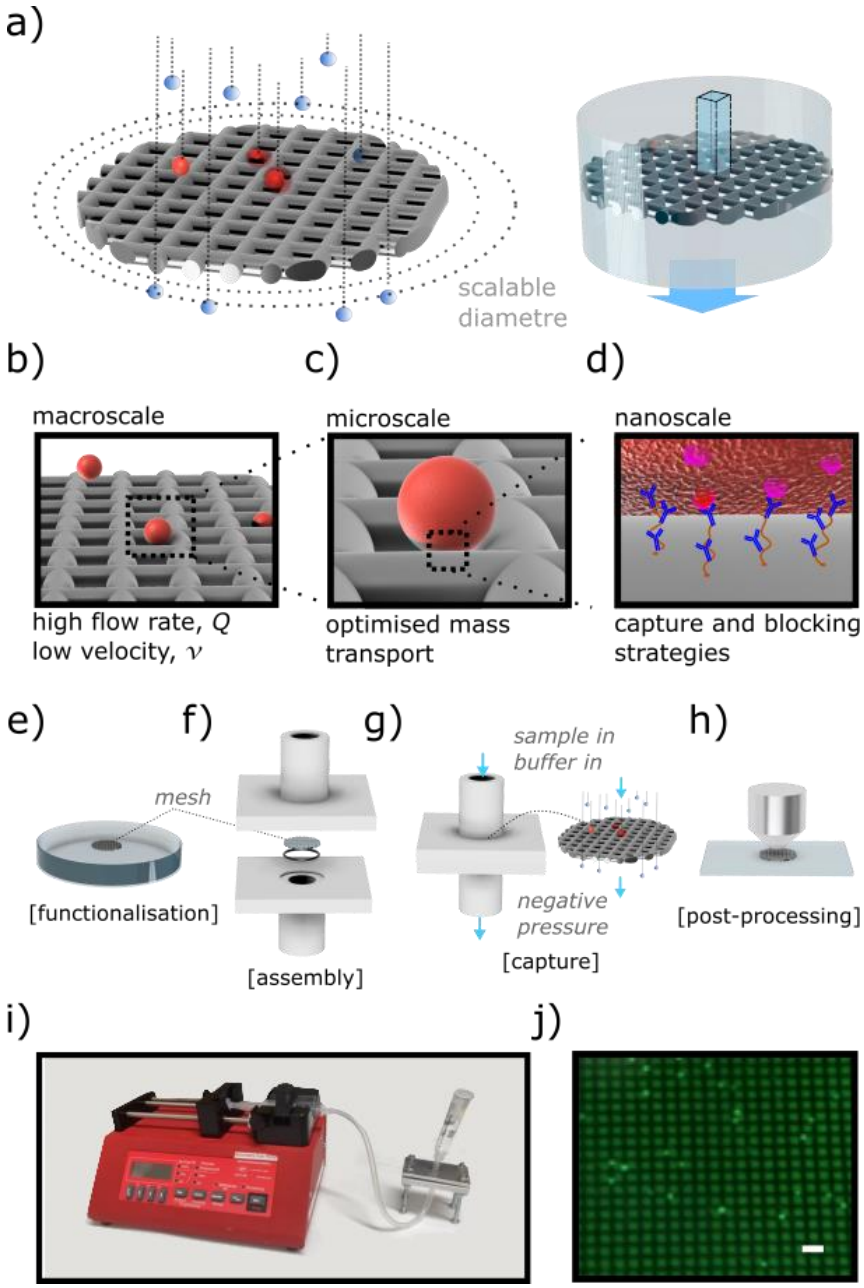

Figure 1. Architecture of the device. The core of the device is a scalable micromesh – not to scale (a) that enables the decoupling and independent optimisation of biosensing-relevant length scales. The resulting device offers a macroscale channel to maintain low fluid velocity while running samples at high flow rate (b), a microscale mesh whose dimension enhances interactions with the target cells (c) and a nano-functionalised coating that enables high capture efficiency and low non-specific interaction (d). The mesh (not to scale) can be represented as thousands of microchannels, optimised for liquid biopsy, in parallel (a, right). The main operations including functionalisation (e), assembly (f), capture (g) and post-processing (h) are made easier by the fact that the mesh can be easily removed from its holder, allowing access for pre- (e) and post-processing (h) as shown in (j) that displays GFP expressing MCF-7 cells observed after capture, scale bar 40 µm. The assay can be performed using widely available laboratory equipment (i).

Third, it allows for easy, off-chip functionalisation before assembly, and importantly, allows for simple post-processing of the captured CTCs. Indeed, the mesh can be easily removed from its holder and manipulated for further processing. It represents a much simpler approach compared to

on-chip processing or cell retrieval. We demonstrate the post-processing capabilities of our device by studying the expression of PD-L1 in CTCs isolated from 33 patients. The expression of PD-L1 in tumor tissues is currently used as a biomarker to predict the response of patients to PD-1 - PD-L1 immune checkpoint inhibition. Using immunofluorescence double-labelling technology, we identified 12 patients (36%) with PD-L1+ CTCs, as potential responders. Then, we evaluate our device against the clinical gold standard for the identification of HER2 (Human epidermal growth factor receptor 2) positive breast cancers, an important prognostic and predictive marker for targeted therapies [21]. Compared to fluorescence in-situ hybridisation (FISH) of patient tumour (solid) biopsies, our device correctly identified HER2 positive CTCs in 80% of cases. These results demonstrate the potential applicability of our simple multiscale, flow rate independent liquid biopsy strategy for cancer management.

Results

Decoupling length scales for optimised flow rate independent capture and device optimisation.

The Peclet number (*Pe*), a dimensionless number that measures the ratio of the convection rate over the diffusion rate, is a transport metric used to optimise biosensors [22–24]. Applied to the context of rare events (such as CTCs in blood), one solution is to keep *Pe* small (<<1) to promote interaction between the target cell and the functionalised surface and maximise cell capture. In most microfluidics publications, the Peclet number is written as $Pe=Q/DL$ (e.g., [22,23,25]), Q being the flow rate, D the diffusion coefficient, and L the characteristic length scale. It is interesting to note that this notation emphasises the flow rate limitation. However, the Peclet number can also be written as $Pe=vL/D$, which suggests that the fluid velocity v may be the true limiting factor, provided it can be decoupled from the flow rate.

In microfluidic channels, flow rate and velocity are coupled via the channel's cross section through $v=Q/A$ (Supp Mat for details). To decouple them, we introduce structures that have two inherent length scales. We use meshes with microscale pore size (for optimised mass transfer) and macroscale diameter (for high flow rate, yet low fluid velocity) mounted in a channel of matching size. In this configuration, the velocity can be kept low for any flow rate. Indeed, it suffices to increase the cross section of the mesh (and channel) A_s to reduce the fluid velocity for a given flow rate, $v=Q/A_s$. This is achieved by simply cutting the mesh to the right diameter. Importantly, this is achieved without compromising the micron-size length scale (pore size), necessary for optimal mass transfer or the nanoscale, critical for functionalisation strategies.

Taking the concept even further, we show how to achieve a flow rate independent capture. Indeed, an arbitrary velocity v_a can be kept constant provided the flow rate and the diameter are scaled by the same factor α as shown in $v_a = \alpha Q_a / \alpha A$. This is demonstrated experimentally by measuring the device's capture efficiency at different flow rates (Fig. 2). The capture efficiency is given by the ratio of the captured to the introduced target cells. We used GFP expressing MCF-7 breast cancer cell line (as shown after capture in Fig 1j) and the functionalisation procedure described below on a 15 x 20 µm pore size mesh. First, we defined the diameter-dependent optimal flow rate Q_o. It is the flow rate yielding the maximum capture efficiency before drop-off, using a mesh with a fixed diameter. A constant capture efficiency of 75% is observed until Q_o = 50 µL min^{-1} before decreasing significantly as shown in Figure 2b (and Fig. SM3 in Supplementary Materials), for a mesh of 6 mm diameter. This behaviour is consistent with other affinity-based liquid biopsies [11,17,19] and with our simulations (Fig. 3). The optimal velocity of our system, $v_o = Q_o/A_s$ (with Q_o = 50 µL min^{-1} and $A_s \cong 88.3\ mm^2$ ($\emptyset = 6\ mm$)) is thus v_o = 2.95 x 10^{-5} m s^{-1}. This velocity can be kept constant for any flow rate provided Q_o and A_s are multiplied by the same factor, α. Figure 2a shows no significant difference in capture efficiency for α = 1 - 4, i.e for flow rates ranging from 50 to 200 µL min^{-1}, as determined by one-way

ANOVA [F=0.37, p=0.05]. A post-hoc Tukey's test shows that there is no statistical difference between any of the flow rates (Fig. SM2). This result is in stark contrast with Figure 2b that shows a strong dependency on the flow rate, as determined by one-way ANOVA [F=38.04, p=0.05], when the diameter of the mesh is kept constant. Graphs with flow rates down to 20 µL min^{-1} (Fig. SM3) and details of the post-hoc Tukey's tests (Fig. SM2, SM4) are provided in Supplementary Materials. More practically, this approach can be used to find an optimum capture efficiency given a target flow rate, Q_t. Indeed, a simple rule of three suffices to define the optimal mesh cross section, A_{st}, as defined by $A_{st} = Q_t/v_0 = A_s\, Q_t/Q_0$ (the initial surface area times the ratio of the target to the initial flow rate).

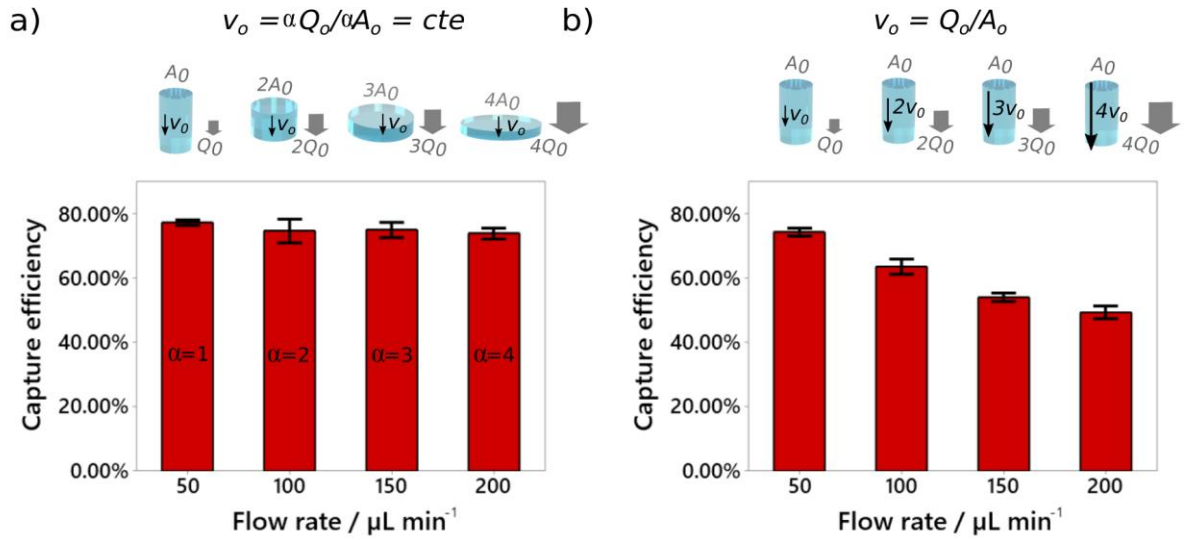

Figure 2. Flow rate independence. Panel (a) shows that capture efficiency can be kept constant (as confirmed by one-way ANOVA [F=0.37, p=0.05] and post-hoc Tukey's test (Fig. SM2)) as long as the velocity is kept constant. This is achieved by scaling the surface area by the same factor as the flow rate as given by $v = \alpha Q/\alpha A$. In comparison, one observes a significant capture efficiency decrease (one-way ANOVA [F=38.04, p=0.05]), when the diameter of the mesh is kept constant (b). The measurements were performed using MCF-7 cell lines spiked in buffer solutions. The bars represent the standard error.

Comparative (semi-quantitative) multiphysics simulations (COMSOL Multiphysics 5.5) were performed to optimise the device (Fig. 3). The effect of the flow rate on the capture efficiency is shown in figures 3a,b, which represent the cross section of a mesh in a channel. Figure 3a displays the reaction of diluted species on the mesh. A diluted solution of particles (arbitrary concentration $C_{0)}$ is represented in red and introduced at the top of the channel at arbitrary flow rates Q_0, $2Q_0$ and $3Q_0$. The background solution is represented in blue ($C_0 = 0$). The blue traces therefore represent the solution depleted from the particles captured on the mesh. The simulations show that the amount of particles captured decreases with increasing flow rate (i.e., less material is captured by the mesh) for a given channel diameter, which confirms our experimental results (Fig 2b). The particle tracing module was used to evaluate the flow rate dependence of the capture efficiency for discrete events, to represent individual cells. Figure 3b shows a representative image (inset) and a graph based on a series of individual repeats and confirms the previous observations (experiments and simulations). In both cases, several mesh parameters, including wire diameter and pore sizes, were evaluated to select the meshes for experimental work. The results provided qualitative data (not shown) whose trend aligned well with experiments. We also used the simulation to optimise the position of the mesh in the device. Figure 3c highlights the effect of channel diameter restrictions, which can locally increase the velocity across a mesh if it is positioned in its proximity. Since an increased velocity reduces the capture efficiency, it is important to position the mesh sufficiently far away from any diameter restrictions.

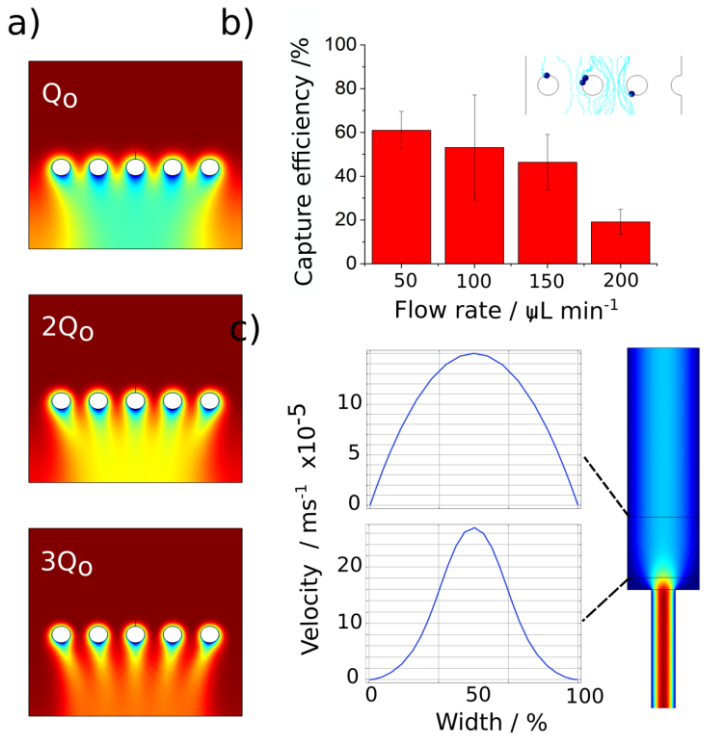

Figure 3: Comparative (semi-quantitative) multiphysics simulations. Panel (a) shows the effect of the flow rate on the capture of diluted species (arbitrary concentration C_0 indicated in red) on the mesh. Here a cross section is represented. A depletion zone (blue) appears for a flow rate Q_0 and decreases progressively as the flow rates are increased ($2Q_0$ and $3\ Q_0$). The same was observed for discrete events, using particle tracing in (b). In this case, we performed individual measurements (at least triplicates) and reported them in a graph to show the flow rate dependency on the capture efficiency. Panel (c) shows the effect of restrictions in the vicinity of the mesh (cross section). If the mesh is too close to a diameter restriction, the velocity increases locally, thereby negatively impacting the capture efficiency.

In summary, our device combines a macroscale channel that enables a high flow rate while maintaining low fluid velocity, a microscale mesh that promotes interaction between the target cells and a nano-functionalised surface, which allows for high capture efficiency and low non-specific interaction (as discussed in the next section). Importantly, these three length scales can be defined and optimised independently. By analogy, each pore of the mesh can be represented as a single microfluidic channel optimised for liquid biopsy. Taking the example of a mesh with 20 x 20 µm pore size, 6 mm diameter mesh with 30% open mesh area as given by the manufacturer, our mesh can be conceptualised as a collection of over 66,000 parallel channels of 20 by 20 µm cross section (Fig 1a).

Nanobranched Polymer and Capture Optimisation.

We used thiol-terminated nanobranched polymers, tethered to a gold coated micromesh, functionalised with antibodies against specific cell surface receptors to confer high capture efficiency, and high specificity to our device. First, we targeted epithelial cell adhesion molecules (EpCAM) that are characteristically overexpressed in a range of epithelial cancers, but not in other blood cells[26]. EpCAM has already been used in a number of affinity-based liquid biopsy studies [11,17,27–29] and therefore provides a good standard for comparison. Nanobranched polymers can

accommodate multiple anti-EpCAM antibodies alongside blocking molecules, increasing the probability of antigen-to-antibody contact and minimising non-specific interaction[29–31].

The simple design of the device enables seamless removal and mounting of the microscale mesh (Fig. 1e-h), such that its functionalisation can take place in optimal conditions, with minimum waste of precious material. Figure 4a represents the simplified polymer synthesis steps. Detailed description of the polymer synthesis and functionalisation steps are given in the Methods. Briefly, gold coated micromeshes were incubated in sulfhydryl hyaluronic acid (HA-SH) for two hours, followed by activation using EDC/NHS in MES buffer (pH=6). After 30 min, anti-EpCAM antibodies were incubated at 37 °C for 2 h to finalise the functionalisation of the mesh. Antibody dosage and incubation times were systematically examined to optimise binding efficiency (Fig. SM5 in Supplementary Materials). After the reaction, blocking molecules were added (1 h incubation time) to reduce non-specific binding (details are provided below).

We first optimised our device using buffer solutions spiked with a known number of EpCAM expressing MCF-7 cells. The capture efficiency of the device is given by the ratio of captured cells to the total number of cells added to the solution. Before capturing, MCF-7 cells were loaded with intra-cellular live cell dye (CFSE) to simplify their counting and differentiation from background. To optimise the cell culture parameters, we compared the effect of different harvest reagents and the influence of passage number on the EpCAM receptor's integrity, by performing flow cytometry and immunostaining (Fig. SM6). Having optimised these parameters, we evaluated the capture efficiency.

A functionalised 6 mm diameter mesh was mounted into the holder with fluidic channel of matching (ϕ = 6 mm) dimension. A syringe pump was then connected to the holder via medical grade tubing. After priming the device with buffer to the top of the mesh, medium spiked with appropriate cells was added to the open reservoir. The solution was then withdrawn through the mesh at a flow rate of 50 µL min^{-1}, which corresponds to the optimal flow rate for a 6 mm diameter mesh as explained above. Next, fresh medium was added to the reservoir to wash off non-specifically bound cells and ensure that only the cells captured by affinity binding stay on the mesh. Finally, the mesh was removed and observed under a microscope to count the captured cells. Figure 4b shows cells captured on the mesh with varying initial cell concentrations. The simplified process steps are shown in Fig. 1e-h (a more detailed version is presented in Fig. SM1).

Capture efficiency of 58% (σ^2 = 6.3%) is obtained with a 20 × 20 µm pore size micromesh (Fig. 4c). In contrast, antibodies tethered directly to the gold coated mesh via Traut reagent result in capture efficiencies below 20% (Fig. SM7). These result are in line with previously reported studies that noted improved capture efficiency when using nanobranched polymers[31]. Figure 4c also shows that the capture efficiency increased with decreasing pore sizes (at 0.05 level, the population means are significantly different, using one-way ANOVA, F=15.12), even though the 10 × 18 µm and 15 × 20 µm pore size meshes cannot be considered statistically different using post-hoc Tukey's test (Fig. SM8). This increased efficiency is attributed to the higher probability of cells interaction with the functionalised surface. Micromeshes with 10 × 18 µm pore sizes result in capture efficiency up to 81.6% (σ^2 = 1.4%), and correspond to typical values reported for a range of affinity-based microfluidic approaches[32,33]. Even though such pore size can also filter larger CTC clusters, they are generally too large for capturing single CTCs [34,35]. This further confirms that the captures observed in our case are due to affinity binding. It is interesting to note that the capture efficiency does not scale linearly with the projected surface area of the mesh, i.e., the active functionalised surface as seen by the cells. The reduction observed for smaller mesh pore size is attributed to higher local velocity due to the decrease in total open area compared to the optimised flow rate for larger pore size. Indeed, the total mesh open area is reduced by 19% with the 10 × 18 µm pore sizes compared to the 20 × 20 µm pore size, resulting in a velocity increase of 24% for the same flow rate. This suggests that the flow rate v_o should be optimised for each pore size.

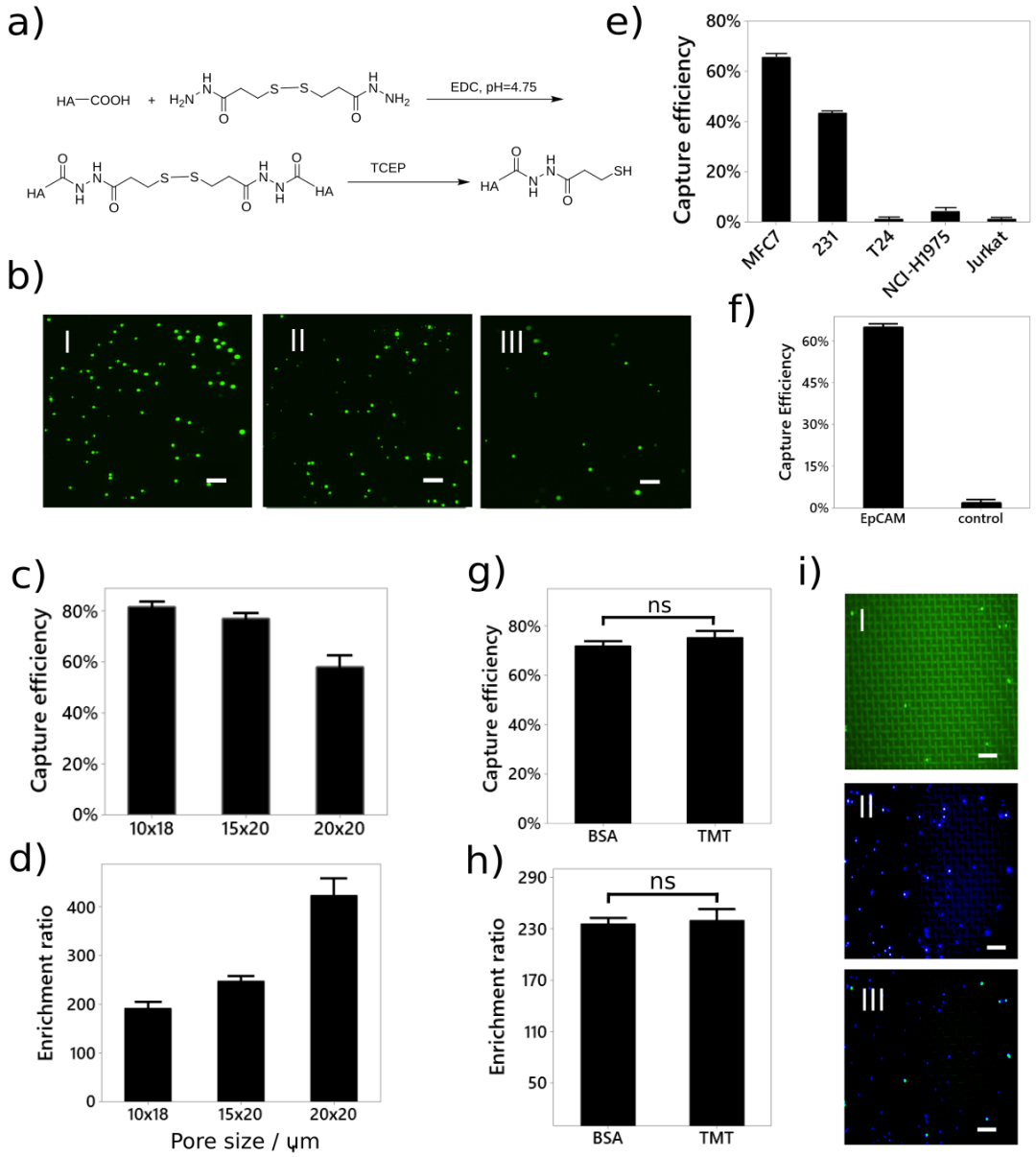

Figure 4. Nano-functionalisation strategies and performance of the device. (a) the nanobranched sulfhydryl hyaluronic acid (HA-SH) synthesis steps. (b) the micrographs of MCF-7 cells on the mesh after being captured with different concentration (approximately 150, 100 and 50 cells per mL for I, II and III respectively) with a scale bar of 200 µm. The effect of different meshes pore sizes (10x18, 15x20 and 20x20 µm) were evaluated on cell capture efficiency (c) and enrichment ratio (d). (e) Different cell lines exhibit capture efficiencies in line with their EpCAM expression levels (shown in Fig. SM9). (f) A control experiment using anti-IgG to replace anti-EpCAM antibodies shows that far fewer MCF-7 cells are captured, confirming the good immunocapture specificity. (g)-(h)Two blocking strategies, using bovine serum albumin (BSA) or trimethoxylsilane (TMT) have shown no significant difference in capture efficiencies or enrichment ratios. (i) shows a typical micrograph of the captured CFSE stained MCF-7 cells (I), DAPI+ cells comprised mostly of background Jurkat cells (II) and merged image (III), the scale bar is 200 µm.

To further evaluate the specificity of our device, we compared the capture efficiency of MCF-7 cells with MDA-MB-231, T24, NCI-H1975 control cells (Fig. 4e). The relative capture efficiencies are in agreement with the EpCAM expression level of each cell type (Fig. SM9). Figure 4f shows that far fewer MCF-7 cells are captured using anti-IgG as control on a 20 × 20 µm pore size micromesh, confirming the good immunocapture specificity of our approach.

Next, we quantified the enrichment of target cell, defined as the ratio of target to background cells detected (on the mesh) divided by the ratio of target to background cells in the sample[10]. For this purpose, we repeated the capture efficiency experiment with the addition of ~1 x 10^6 Jurkat cells (EpCAM -), corresponding to a ratio of about 1:10^4 MCF-7: Jurkat cells. Using BSA (1%) as blocking molecules, enrichment ratios corresponding to 192, 248 and 424 were observed for 10 × 18 µm, 15 × 20 µm and 20 x 20 µm pore size meshes, respectively. These values are similar to a number of affinity-based liquid biopsies[33,36]. The population means are significantly different at 0.05 level, using one-way ANOVA, F=28.04, confirming a reduction in non-specific interaction with decreasing total functionalised area, as expected. However, a post-hoc Tukey's test reveals that the 10 × 18 µm and 15 × 20 µm pore size mesh cannot be considered statistically different. This can be attributed to a combination of the increase in velocity reported above for the 10 × 18 µm pore size mesh that reduces interaction probability and the associated increased shear stress that promotes removal of non-specifically bound cells[11,38].

We then evaluated the effect of trimethoxylsilane (50%) blocking molecules instead of BSA. Using the approach reported above, we did not observe any significant improvement in enrichment (Fig. 4h) or changes in capture efficiency (Fig. 4g) for meshes with 15 x 20 µm pore size. It is also noted that there is no significant difference in capture efficiency between the measurement with and without background cells in the same conditions ($t(4) = 1.0409$; $p = 0.3567$).

Overall, these results confirm that our nanoscale functionalisation strategy is compatible with our device and enables high capture efficiencies and enrichments comparable to a number of existing liquid biopsy technologies, without some of the limitations normally associated with affinity-based liquid biopsies.

Validation Using Clinical Samples

Having characterised the performance of our novel device with immortalised cell lines, we validated its utility using clinical samples. In brief, we evaluated its performance in the first step of our study, then evaluated its post-processing capabilities using a subset of patients (step 2) and finally compared it with clinical standards in a third step. Importantly, we note the simplicity of our set-up that can be integrated in clinical settings with minimum disruption to conventional workflows. The device only requires a single syringe pump to operate. The mesh can be easily removed from its holder, greatly simplifying pre- and post-processing procedures. In addition to relying on conventional and widely available equipment and consumables such as Petri dishes and incubators for conventional functionalisation, the post-processing imaging can be directly performed on the stained meshes using epifluorescence microscopy (Fig. 1e-h).

First, we recruited 79 cancer patients and 20 healthy controls from Fudan University Shanghai Cancer Center and Changzheng hospital (ethical approval #050432-4-1911D). Demographic details of the study population are given in Table SM1. To evaluate the applicability of our device and to reflect the diversity of clinical cases that could benefit from liquid biopsy, we have selected patients with 10 different cancers, including non-small cell lung cancer and breast cancer. The volume of blood sampled was 4 mL. Meshes with 20 x 15 um pore size, 6 mm diameter, and HA-SH polymer with BSA blocking were used with the optimised flow rate of 50 µL min^{-1} (as described above).

The cells captured on the mesh (by the anti EpCAM antibody), staining for $CK^+/CD45^-/DAPI^+$, were identified as CTCs. Among the cancer patients, 96% (76/79) had at least one CTC and about 4% (3/79) had more than 10 CTCs. Using the same enumeration criteria, we tested the healthy controls and detected no CTCs (20/20). The results are summarised in Figure 5a. Using 30% as training set and 70% for classification by logistic regression, we calculated the sensitivity (96%) and specificity (100%) of our device. As confirmation, we generated the receiver operation characteristic (ROC) that

yielded an area under the curve (AUC) value of 0.979 (not shown). These excellent values are due to the dual selection (immuno-capture and staining) inherent to our assay and are in line with results reported for devices using similar approaches [e.g., [11]].

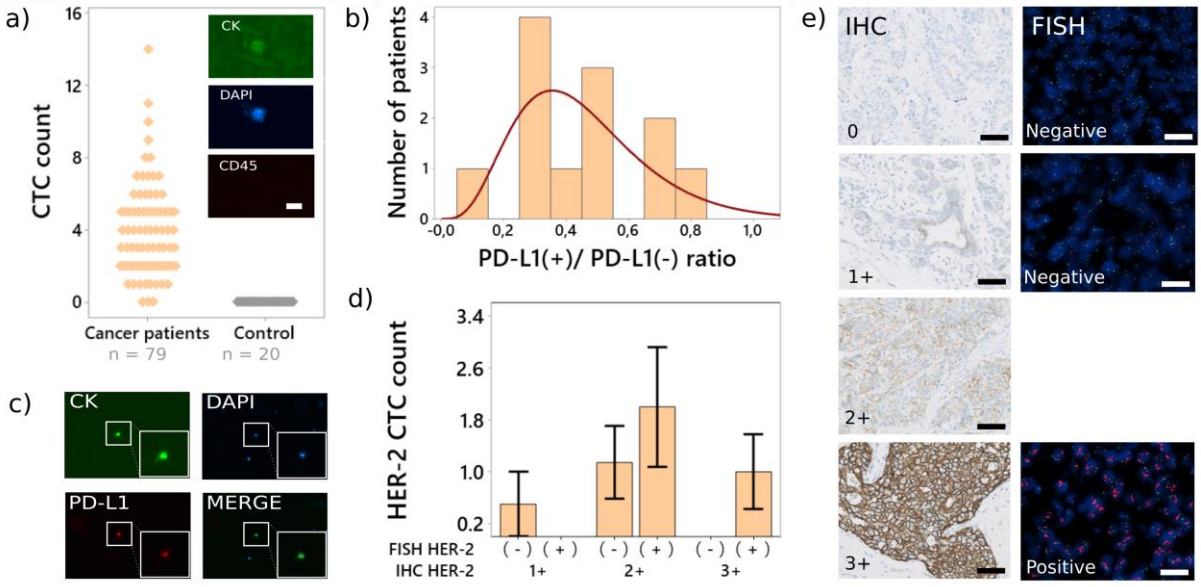

Figure 5. Clinical validation of the device on two cohorts, in three separate studies. The first study, shown in panel (a), with 79 cancer patients with a range of different cancer types and 20 healthy controls was used to characterise the performance of our device. CK+; DAPI+; CK- cells were identified as CTCs (inset), scale bar 20 µm. A subset of patients (n=33) from the initial cohort were selected to evaluate PD-L1 expression to identify potential responders to immune checkpoint inhibition therapy. The distribution of PD-L1+ CTCs to CTCs is shown in (b). PD-L1 expression was evaluated using standard secondary immunostaining (c), scale bar 100 µm. To evaluate our device against clinical standards, we selected 26 breast cancer patients and tested them for HER2 positivity using secondary immunostaining post-processing. We compared our results (d) with the histological scoring of IHC and FISH, two standard clinical assays. Representative images, with scale bar 40 µm, are shown in (e).

In the past decade, studies on CTCs have gone beyond simple enumeration. The analysis of feature-rich CTCs, that may possess attributes of the primary tumour as well as metastasis, can provide clinically actionable information[1–4]. For example, the expression of PD-L1 in tumour tissues, used as a biomarker for the selection of patients eligible for immune checkpoint inhibition (ICI) therapy, is also evaluated using CTCs[38–40]. The upregulation of PD-L1 enables cancer cells to evade immune response by inhibiting the activation of immune cells. ICI therapies target anti PD-L1/PD1 proteins to block the inhibition of immune cells, thereby reactivating the immune system. To further demonstrate the applicability of our device in this clinical context and, in particular, to evaluate its post-processing capabilities, we selected 33 patients from the original cohort (n=79) for the evaluation of PD-L1 expression using immunofluorescence labelling (Fig. 5B,C). This step was performed after isolation of CTCs using anti-EpCAM antibodies as described earlier. On this basis, 36% of patients (12/33) had PD-L1 expressing cells. Among them, the largest proportion of patients (n=4) only had 30% of PD-L1+ CTCs as shown in Figure 5b. Based on the data from the NSCLC patient (n=21), we detected a median of 4 CTCs per 4 mL (range: 2-9 CTCs per 4 mL), among which 48% (n=10) harboured at least one PD-L1+ CTC. The total number of CTCs in 4 mL compares well with at least 2 commercial systems[41] and confirms the efficacy of our approach.

For a final validation study, we used our device to identify HER2 positive breast cancer patients based on the detection of HER2 positive CTCs. We compared our results with IHC and FISH, two

standard methods approved by the U.S. Food and Drug Administration (FDA). HER2 protein overexpression and/or HER2 gene amplification, is found in about 20% of breast cancers and is associated with tumorigenesis, increased risk of metastasis, and poor prognosis[42,43]. Importantly, these markers can be used to identify patients that could benefit from targeted therapies such as Trastuzumab, Pertuzumab and T-DM1. In this study, we selected 26 breast cancer patients from the initial cohort (n=79). They were tested for HER2 status using clinical standard procedures (IHC and FISH) performed on tissue (solid) biopsies and compared with HER2 positive CTCs captured using our device (liquid biopsy). IHC is typically used as a screening test with IHC 0 and IHC 1+ considered as negative, IHC 2+ equivocal and IHC 3+ as positive (Fig. 5d). FISH is considered more reliable, but it is more complicated and expensive, and is therefore normally used to determine the status of IHC 2+ equivocal cases[42–44].

The CTCs were captured using the protocol described for the PD-L1 study, with fluorescently labelled anti-ErbB2 / HER2 antibodies. The results are summarised in Figure 5c. According to the above criteria, 10 patients were identified as HER2 positive using standard approaches (IHC and/or FISH) against 14 identified based on the HER2 positive CTCs. The data shows a consistency (positive rate) of 54.17% (13/24) with the IHC and 80% (8/10, p = 0.0156) with FISH (Table 1). It is a promising result especially since FISH is considered a superior assay. We also note that our device captured HER2+ CTCs when the FISH or even IHC assay produced non-equivocal negative results (7 and 1 respectively). Similar results were reported elsewhere [45].

Table 1: Comparison between the clinical standards (IHC and FISH) and our device.

Subject	Patients	Patients with HER-2 positive CTC	Positive rate	*Chi-square p*
HER2 IHC				0.8921
1+	2	1	50.0%	
2+	21	11	52.4%	
3+	3	2	66.7%	
HER2 FISH				**0.0156**
(-)	16	5	31.3%	
(+)	10	8	80.0%	

In summary, these results demonstrate the applicability of our device in clinical settings. Its versatility and performance were characterised in a three-part study. We demonstrated its post-processing capabilities in the context of PD1/PD-L1 ICI therapies and evaluated it against clinical standards in a HER2 positive breast cancer study.

Discussion

We have characterised and validated the utility of a new multiscale enrichment device that enables flow-rate-independent capture and processing of CTCs. We have achieved this by introducing a mesh structure that has two inherent length scales and, thus, eliminates flow rate as the main limiting factor in affinity-based liquid biopsy. The resulting device offers 1) a macroscale channel to run samples at high flow rate while maintaining low fluid velocity, 2) a microscale mesh that promotes interaction with the target cells and a 3) nano-functionalised surface that enables high capture efficiency and low non-specific interaction. Using micromeshes with 15 x 20 µm pore size and HA-SH nanobranched polymer, we have reached >76% capture efficiency, which is comparable to a number

of microfluidics based liquid biopsies[32,33]. However, unlike conventional microfluidics approaches, we have also demonstrated how our device can be scaled to allow for optimal capture efficiency for any flow rate. In particular, we have demonstrated constant capture efficiencies up to 75% at 12 mL h^{-1} (200 µL min^{-1}). Even though our assays did not necessitate higher flow rates, it is noted that it should be possible to further increase it rate by scaling the mesh diameters appropriately.

Importantly, our device is easy to fabricate and assemble, its operation does not require specialist equipment and its architecture allows for simple pre- and post-processing. Hence, our approach can be seamlessly integrated into conventional laboratory workflows, including in demanding clinical environments. To demonstrate this, we validated our device using clinical samples. After capture on the mesh, the cells that stained CK+/CD45−/DAPI+ were identified as CTCs. Following these criteria, we positively enumerated CTCs in all blood samples (4 mL) from cancer patients (n=79). Using data from 20 healthy donors as control, our device yielded 96% sensitivity and 100% specificity, which is comparable to other approaches relying on a combination of capture and staining[11,47]. To further demonstrate the post-processing capabilities of the device, we selected 33 patients to detect PD-L1+ CTCs using secondary immunostaining. PD-L1, a marker for ICI therapies, was expressed in at least one CTC of 36% of the patients. In comparison to commercially available liquid biopsy approaches, in the context of non-small-cell lung carcinoma, our device performed favourably[41]. Finally, we validated our approach against clinical standards in the context of HER2 positive breast cancer on a cohort of 26 breast cancer patients. In particular, we observed an 80% correspondence with FISH positive results. The identification of HER2 positive CTCs in 14 patients overall was higher than the number of patients (n=10) identified as HER2 positive based on the standard methods. Similar findings were reported elsewhere[45] and may be due to intra-tumoral HER2 heterogeneity[44]. More studies, beyond the scope of this manuscript, will be necessary to evaluate the clinical relevance of HER2+ CTCs.

At this stage, it is worth noting the differences and complementarity of our approach in relation to capture methods based on the physical properties of CTCs. Strategies relying on size differences to discriminate cancer cells from healthy blood cells have recently gained in popularity due to their simplicity and high throughput[3]. However, it is accepted that such approaches may miss small-sized CTCs[47] that are correlated with aggressive metastatic progression in patients[49]. Therefore, our approach offers an affinity-based alternative, that harbours identical simplicity and throughput.

Finally, we also note that our functionalisation strategy is compatible with the addition of further antibodies or capture molecules for improved cell isolation efficiency[50] but also for other liquid biopsies. Indeed, our approach can be adapted to other cell types, vesicles, and biomolecules (as done elsewhere, e.g., [3,13,50,51]) in a range of complex fluids. In addition, our nanobranched polymer is amenable to modification and may allow for the integration of cell release strategies (e.g., [20,30]), which will enable further downstream analysis including next generation sequencing. In conclusion, our multiscale, flow-rate-independent multiscale liquid biopsy approach has the potential to help drive significant advances in diagnosis, prognosis, and fundamental studies for a range of conditions.

Materials and methods

Device fabrication and preparation

*Fabrication***.** Micromeshes of different pore sizes (10 x 18, 15 x 20 and 20 x 20 µm) were obtained from Zhongxin Hairu Ltd, China (Cat. No.: 1000 635, 800 635, 635 635, respectively). Prior to coating they were cleaned in 30% ethanol using ultrasound for 5 minutes, rinsed in deionized water and then dried using nitrogen (N_2). Meshes were gold coated (50 nm both sides) using magnetron

sputtering and cut to size (e.g., 8.8 mm diameter mesh for the 6 mm diameter mesh holder) using clean surgical forceps. The mesh holders were fabricated using 3D printing or conventional machining. The mesh holders (Fig. 1 and Fig SM10) comprise groves to accommodate a gasket. Screws or a clamping mechanism held the mesh in place during use.
Preparation and cleaning of the mesh. MilliQ water, 25% Ammonium hydroxide, 30% Hydrogen peroxide were mixed in a clean beaker (5:1:1 ratio, respectively) and heated to 75°C. The cut meshes were submersed for 5 minutes and washed in MilliQ water and 99% ethanol before drying with N_2 and then transferred into a clean petri dish for functionalisation.

Nanofunctionalisation
HA-SH nanobranched polymer synthesis. 40 mL MES solution (Aladdin, Cat. No.: M108952, pH = 4.75, 0.1 M), was slowly added into the single-mouth flask. 200 mg sodium hyaluronate (Bloomage BioTechnology, Cat. No.: HA-TLM, molecular weight: 3.9 W) was then added into the flask and stirred (magnetic stirrer 400 rpm) until the sodium hyaluronate was fully dissolved (5-8 minutes). Then, 60 mg DTP (Frontier scientific, Cat. No.: D13817) was added into the flask and stirred thoroughly until completely dissolved. 120 mg EDC (Sinoreagent, Cat. No.: 30083834) powder was added into the solution which was then stirred at 400 rpm at room temperature for 5 h. Finally, 150 mg TCEP (Sigma, Cat. No.: C4706) was added into solution. After overnight (about 16 h) stirring, the sulfhydryl hyaluronic acid (HA-SH) was filtered (0.22 µm filter) and collected.

Mesh functionalisation. Clean meshes (up to 18) were submerged in 3 mL HA-SH in a 5 mL centrifuge tube and orbital shook at 200 rpm for 2 h to form thiol-Au bonds between HA-SH and the mesh. After washing three time with 3 mL PBS, the meshes were submerged in 3 mL SH-PEG-COOH (Toyongbio, Cat. No.: P003002) for 1 hour to react the unbonded Au. Then the meshes were washed three times with 3 mL PBS, dried and put in a 24 well plate (one mesh per well). Activating reagents (55 µL per mesh in MES (pH = 6, 0.05 M)), comprised of 1-(3-dimethyl aminopropyl)-3-ethyl carbodiimide (EDC, Sigma, Cat. No.: 03449): 0.609 mg / mesh (35 µL) and n-hydroxysuccinimide (NHS, Sigma, Cat. No.: 56485): 0.348 mg / mesh (20 µL), were added to the surface of each HA-SH functionalised gold mesh and incubated at room temperature for 30 minutes. After incubation, the gold meshes were removed and washed three times with 500 µL PBS. The meshes were then dried and moved to new 24-well plate. The capture solution was prepared by adding 7 µL anti-EpCAM antibody (1:2000, #324202, Biolegend, CA US) to 50 µL MES (pH = 6, 0.05 M) solution and subsequent vortexing. The capture solution (57 µL) was then added onto a mesh and placed at 37°C and 5% CO_2 in an incubator for two hours to allow for an amide bond to be created between the anti-EpCAM antibody and HA-SH. Then, the mesh was removed and washed twice with 1 mL PBS. A blocking solution to minimise non-specific interaction (450 µL of 1% BSA solution (w/v%) – Sigma (B2064-50G)) was added to the gold mesh and returned to the incubator for one hour. After washing with PBS (Hyclone), meshes were submerged in 500 µL cryoprotectant (45% sucrose (w/v%, Sinoreagent, Cat. No.: 10021463) and 15% glycin (w/v%, Sinoreagent, Cat. No.: 62011516) in Tris-HCL (Sangon Biotech, Cat. No.: B548127-0500, 1 M, pH = 8.0)), pre-cooled to -20°C for at least one hour until it was solidified and then lyophilized. The lyophilized mesh was then sealed with desiccant and stored at -20°C ready for use.

Cell culture and labelling
Cell culture: Human breast cancer (MCF-7, MDA-MB-231), urinary bladder (T24), lung (NCl-H1975) and monocytic (Jurkat) cells were obtained from iCell (China). All cells were cultured as recommended using phenol-red free Dulbecco's modified Eagle's medium (DMEM) (Gibco, NY, U.S.A.) supplemented with 1% l-glutamine (Life Technologies, CA, U.S.A.), 10% Fetal Bovine Serum (FBS, Gibco), and 1% penicillin/streptomycin (Corning, VA, U.S.A.), with the exception of MCF-7 which were grown in 50:50 phenol-red free DMEM:Nutrient Mixture F12 (DMEM:F12, Gibco) supplemented with 1X B27 (Gibco), 5 mg/l insulin (MBL International Corp., MA, U.S.A.), 20 µg/L

basic fibroblast growth factor (bFGF, Shenandoah Inc., PA, U.S.A.), 20 µg/L epidermal growth factor (EGF, Shenandoah Inc., PA, U.S.A.), 1% penicillin/streptomycin (Corning, VA, U.S.A.), 0.5 mg/l hydrocortisone (Sigma Aldrich, MO, U.S.A.), and 2.5 mM L-glutamine (Life Technologies, U.S.A.).

Cell labelling: For staining, cells were trypsinised and washed twice with PBS before being stained with cell tracker (CellTrace™ CFSE Cell Proliferation Kit) following the manufacturer instructions and resuspending cells in 1ml culture media. Green fluorescent protein (GFP) expressing MCF-7 cells were generated by lentiviral transduction with pWPI as previously described [52]

EpCAM expression. Flow cytometry was performed using BD Accuri C6 Flow Cytometer (BD Biosciences, U.S.A.). EpCAM mouse anti-human FITC conjugated antibody was used for epithelial marker expression (cat. # 347197, BD Bioscience, U.S.A.).

Spiking assay. MCF-7 cells grown in log phase were digested with trypsin (Life Technologies, U.S.A.), washed 2-3 times with phosphate buffer. Then, cells were accurately obtained with a cell counter and mixed into 4 mL buffer.

Material from clinical studies.
Cancer patients and control groups were recruited at Fudan University Shanghai Cancer Center and Changzheng Hospital, China (ethical approval #050432-4-1911D) after providing informed consent. Patients in this cohort may have received preoperative surgery or systematic anticancer treatment but must have been enrolled in this cohort at least 30 days in advance.

For processing in our novel devices, at least 4 mL blood of cancer patients and healthy individuals were collected and stored in EDTA tubes, blood was tested within 6 hours. Before detection of CTC, blood was processed according to the local clinical standard. Briefly, blood was diluted 1:1 in PBS (pH = 7.0) and then carefully transferred to a sterile 15 mL centrifuge tube which contained pre-warmed density gradient separation solution (4 mL, Dakewe Biotech, Shenzhen, China). This layered liquid tube was centrifuged with 700 g at room temperature for 20 minutes. The PBMC layer was pipetted into a new sterile 15 mL centrifuge tube and washed with PBS, twice (500 g, 5 minutes), and finally the PBMCs were resuspended in 300 µL PBS before use in the device.

The mesh-bound cells were fixed with 4% paraformaldehyde and washed with PBS. The fixed cells were infiltrated with 1% NP40 and blocked with 2% normal goat serum / 3% BSA. Staining to identify CTCs was performed using well established protocols using pan-Ck (Alexa Fluor488 anti-Cytokeratin (CK, pan-reactive) antibody, Biolegend (628608)), CD45 (PE anti-human CD45 Antibody, Biolegend (304008)) and DAPI (Sigma (D9542)). Secondary immunofluorescence labelled antibodies were used for the identification of PD-L1 positive cells: anti-human PD-L1 (Biolegend: 329708). Alexa Fluor 647 Anti-ErbB2 / HER2 antibody [EPR19547-12] (ab225510) was used for the identification of HER2 positive CTCs. After staining, the plate was washed with PBS and stored at 4°C until microscopic imaging.

Tissue embedding sectioning. The fresh patient biopsies were fixed in 4% formalin/paraformaldehyde, dehydrated in an ethanol series. After clearing in xylene, samples were infiltrated with paraffin wax. The wax block was cooled at -20°C and sliced on a microtome in 4 µm sections. For immunostaining and FISH, sections were mounted, deparaffinized and rehydrated.

Immunohistochemistry (IHC): Antigens were recovered in citric acid (pH 6) buffer, and endogenous peroxidase activity as well as unspecific binding were blocked by transferring the sections into 3% BSA buffer. After 30 min, BSA was removed and sections were incubated with primary antibody (1:200, Alexa Fluor® 647 Anti-ErbB2 / HER2 antibody [EP1045Y] (ab281578, Abcam, British)). After

overnight incubation at 4°C sections were washed with PBS, and the secondary antibody (1:1000, Goat-Anti-Rabbit-HRP labelled, Servicebio, China) was applied at room temperature for 50 min. Again, sections were washed with PBS and stained with DAB staining kit (G1211, Servicebio, China), according to the manufacturer instructions. Nuclei in the sections were counterstained with hematoxylin. After being dehydrated and mounted, the stained tissue sections were visualized using a light microscope at x20 magnification.

Fluorescence in situ hybridisation (FISH) protocol. The FDA approved PathVysion HER2 DNA probe kit (Abbott Molecular, IL, U.S.A.) was used according to the manufacturer protocols. Briefly, DNA on slides was denatured at 72±1°C for 5 minutes and then were washed and desiccated. After that 10 µL of probe mixture was applied in a pre-warmed humidified hybridisation chamber at 37±1°C for 14 to 18 h. After hybridisation, the sections were washed with SSC at 72±1°C and desiccated in the dark. 10 µL of DAPI was applied to counterstain the sections area of the slide. Sections were observed under a fluorescence microscope. The analyses of IHC and FISH were obtained from clinicians according to clinical guidelines.

Statistical analysis.
Results were analysed using Student's two tailed t-test, and ANOVA with equal or unequal variance in Minitab 19 (Minitab Inc., State College, PA, U.S.A.). Differences with p-values <0.05 were considered significant, and post-hoc Tukey's tests were performed after significant ANOVA differences. The logistic regression and ROC curves were obtained using the scikit-learn Python package (Python 3, on Jupyter Notebook).

Multiphysics simulation
We used COMSOL Multiphysics (version 5.5) to conduct our simulations. To evaluate the effect of the flow rate on capture efficiency (Fig 3a), we used the "Creeping flow" and "Transport Diluted Species" modules with mesh boundary conditions (General Form Boundary PDE) to include a local Langmuir adsorption model as explained elsewhere[53]. To evaluate time-dependent discrete events (Fig3b) we selected the "Creeping flow" and "Particle tracing for Fluid flow' modules. A 'pass through' boundary condition was set on the outer perimeters of the channel, and a 'stick' condition for the mesh, so particle-wall interactions could easily be determined visually. The study on the flow velocity (Fig. 3c) was done using the Creeping flow module. Each study was repeated at least four times.

Authors contribution

Conceptualisation: JY, JC. Investigation, methodology: JW, JY, RD, RL, JC. Validation: RL, YJ, RD, JC. Writing – original draft: JY, JC. Writing – review and editing: all.

Conflict of interest

The work presented in this manuscript resulted in three patent applications by Holosensor Medical Ltd. The research was partly funded by Holosensor Medical Ltd. J. Y. is employed by Holosensor Medical Ltd. The remaining authors declare that the research was conducted in the absence of any commercial or financial relationships that could be construed as a potential conflict of interest.

Ethics statement

The study was conducted in accordance with the Declaration of Helsinki (as revised in 2013). The study was approved by the Ethics Committee of Fudan University Shanghai Cancer Center and Changzheng hospital, individual consent for this study was waived.

Acknowledgements

JC would like to acknowledge funding from the Newton Fund—Institutional Links grant (ID 352360246), and Engineering and Physical Sciences Research Council grant EPSRC EP/R00403X/1. We are grateful to Hannah Bridgewater for fruitful discussions and Helena Xandri-Monje, Hadi Putra, Sunil Prasanan and Joseph Parker for contributions to initial experiments and optimisation. Our gratitude goes to Professor Yin of Changzheng Hospital for sample contribution.

References

(1) Pantel, K.; Alix-Panabières, C. Liquid Biopsy and Minimal Residual Disease — Latest Advances and Implications for Cure. *Nat. Rev. Clin. Oncol.* **2019**, *16* (7), 409–424. https://doi.org/10.1038/s41571-019-0187-3.

(2) Pappas, D. Microfluidics and Cancer Analysis: Cell Separation, Cell/Tissue Culture, Cell Mechanics, and Integrated Analysis Systems. *Analyst* **2016**, *141* (2), 525–535. https://doi.org/10.1039/C5AN01778E.

(3) Vaidyanathan, R.; Hao Soon, R.; Zhang, P.; Jiang, K.; Teck Lim, C. Cancer Diagnosis: From Tumor to Liquid Biopsy and Beyond. *Lab. Chip* **2019**, *19* (1), 11–34. https://doi.org/10.1039/C8LC00684A.

(4) Zhou, E.; Li, Y.; Wu, F.; Guo, M.; Xu, J.; Wang, S.; Tan, Q.; Ma, P.; Song, S.; Jin, Y. Circulating Extracellular Vesicles Are Effective Biomarkers for Predicting Response to Cancer Therapy. *EBioMedicine* **2021**, *67*, 103365. https://doi.org/10.1016/j.ebiom.2021.103365.

(5) Kim, M.-Y.; Oskarsson, T.; Acharyya, S.; Nguyen, D. X.; Zhang, X. H.-F.; Norton, L.; Massagué, J. Tumor Self-Seeding by Circulating Cancer Cells. *Cell* **2009**, *139* (7), 1315–1326. https://doi.org/10.1016/j.cell.2009.11.025.

(6) Krebs, M.; Szczepaniak Sloane, R.; Priest, L.; Lancashire, L.; Hou, J.-M.; Greystoke, A.; Ward, T.; Ferraldeschi, R.; Hughes, A.; Clack, G.; Ranson, M.; Dive, C.; Blackhall, F. Evaluation and Prognostic Significance of Circulating Tumor Cells in Patients With Non-Small-Cell Lung Cancer. *J. Clin. Oncol. Off. J. Am. Soc. Clin. Oncol.* **2011**, *29*, 1556–1563. https://doi.org/10.1200/JCO.2010.28.7045.

(7) Denève, E.; Riethdorf, S.; Ramos, J.; Nocca, D.; Coffy, A.; Daurès, J.-P.; Maudelonde, T.; Fabre, J.-M.; Pantel, K.; Alix-Panabières, C. Capture of Viable Circulating Tumor Cells in the Liver of Colorectal Cancer Patients. *Clin. Chem.* **2013**, *59* (9), 1384–1392. https://doi.org/10.1373/clinchem.2013.202846.

(8) Burz, C.; Pop, V.-V.; Buiga, R.; Daniel, S.; Samasca, G.; Aldea, C.; Lupan, I. Circulating Tumor Cells in Clinical Research and Monitoring Patients with Colorectal Cancer. *Oncotarget* **2018**, *9* (36), 24561–24571. https://doi.org/10.18632/oncotarget.25337.

(9) Eslami-S, Z.; Cortés-Hernández, L. E.; Thomas, F.; Pantel, K.; Alix-Panabières, C. Functional Analysis of Circulating Tumour Cells: The KEY to Understand the Biology of the Metastatic Cascade. *Br. J. Cancer* **2022**, 1–11. https://doi.org/10.1038/s41416-022-01819-1.

(10) Ferreira, M. M.; Ramani, V. C.; Jeffrey, S. S. Circulating Tumor Cell Technologies. *Mol. Oncol.* **2016**, *10* (3), 374–394. https://doi.org/10.1016/j.molonc.2016.01.007.

(11) Nagrath, S.; Sequist, L. V.; Maheswaran, S.; Bell, D. W.; Irimia, D.; Ulkus, L.; Smith, M. R.; Kwak, E. L.; Digumarthy, S.; Muzikansky, A.; Ryan, P.; Balis, U. J.; Tompkins, R. G.; Haber, D. A.; Toner, M. Isolation of Rare Circulating Tumour Cells in Cancer Patients by Microchip Technology. *Nature* **2007**, *450* (7173), 1235–1239. https://doi.org/10.1038/nature06385.

(12) Fischer, J. C.; Niederacher, D.; Topp, S. A.; Honisch, E.; Schumacher, S.; Schmitz, N.; Föhrding, L. Z.; Vay, C.; Hoffmann, I.; Kasprowicz, N. S.; Hepp, P. G.; Mohrmann, S.; Nitz, U.; Stresemann, A.; Krahn, T.; Henze, T.; Griebsch, E.; Raba, K.; Rox, J. M.; Wenzel, F.; Sproll, C.; Janni, W.; Fehm, T.; Klein,

C. A.; Knoefel, W. T.; Stoecklein, N. H. Diagnostic Leukapheresis Enables Reliable Detection of Circulating Tumor Cells of Nonmetastatic Cancer Patients. *Proc. Natl. Acad. Sci.* **2013**, *110* (41), 16580–16585. https://doi.org/10.1073/pnas.1313594110.

(13) Hao, N.; Zhang, J. X. J. Microfluidic Screening of Circulating Tumor Biomarkers toward Liquid Biopsy. *Sep. Purif. Rev.* **2018**, *47* (1), 19–48. https://doi.org/10.1080/15422119.2017.1320763.

(14) Mao, S.; Zhang, Q.; Li, H.; Zhang, W.; Huang, Q.; Khan, M.; Lin, J.-M. Adhesion Analysis of Single Circulating Tumor Cells on a Base Layer of Endothelial Cells Using Open Microfluidics. *Chem. Sci.* **2018**, *9* (39), 7694–7699. https://doi.org/10.1039/C8SC03027H.

(15) Alix-Panabières, C.; Pantel, K. Circulating Tumor Cells: Liquid Biopsy of Cancer. *Clin. Chem.* **2013**, *59* (1), 110–118. https://doi.org/10.1373/clinchem.2012.194258.

(16) Belotti, Y.; Lim, C. T. Microfluidics for Liquid Biopsies: Recent Advances, Current Challenges, and Future Directions. *Anal. Chem.* **2021**, *93* (11), 4727–4738. https://doi.org/10.1021/acs.analchem.1c00410.

(17) Shen, Q.; Xu, L.; Zhao, L.; Wu, D.; Fan, Y.; Zhou, Y.; OuYang, W.-H.; Xu, X.; Zhang, Z.; Song, M.; Lee, T.; Garcia, M. A.; Xiong, B.; Hou, S.; Tseng, H.-R.; Fang, X. Specific Capture and Release of Circulating Tumor Cells Using Aptamer-Modified Nanosubstrates. *Adv. Mater.* **2013**, *25* (16), 2368–2373. https://doi.org/10.1002/adma.201300082.

(18) Lu, Y.-T.; Zhao, L.; Shen, Q.; Garcia, M. A.; Wu, D.; Hou, S.; Song, M.; Xu, X.; OuYang, W.-H.; OuYang, W. W.-L.; Lichterman, J.; Luo, Z.; Xuan, X.; Huang, J.; Chung, L. W. K.; Rettig, M.; Tseng, H.-R.; Shao, C.; Posadas, E. M. NanoVelcro Chip for CTC Enumeration in Prostate Cancer Patients. *Methods* **2013**, *64* (2), 144–152. https://doi.org/10.1016/j.ymeth.2013.06.019.

(19) Pahattuge, T. N.; Freed, I. M.; Hupert, M. L.; Vaidyanathan, S.; Childers, K.; Witek, M. A.; Weerakoon-Ratnayake, K.; Park, D.; Kasi, A.; Al-Kasspooles, M. F.; Murphy, M. C.; Soper, S. A. System Modularity Chip for Analysis of Rare Targets (SMART-Chip): Liquid Biopsy Samples. *ACS Sens.* **2021**, *6* (5), 1831–1839. https://doi.org/10.1021/acssensors.0c02728.

(20) Wang, S.; Liu, K.; Liu, J.; Yu, Z. T.-F.; Xu, X.; Zhao, L.; Lee, T.; Lee, E. K.; Reiss, J.; Lee, Y.-K.; Chung, L. W. K.; Huang, J.; Rettig, M.; Seligson, D.; Duraiswamy, K. N.; Shen, C. K.-F.; Tseng, H.-R. Highly Efficient Capture of Circulating Tumor Cells by Using Nanostructured Silicon Substrates with Integrated Chaotic Micromixers. *Angew. Chem.* **2011**, *123* (13), 3140–3144. https://doi.org/10.1002/ange.201005853.

(21) Park, M.-H.; Reátegui, E.; Li, W.; Tessier, S. N.; Wong, K. H. K.; Jensen, A. E.; Thapar, V.; Ting, D.; Toner, M.; Stott, S. L.; Hammond, P. T. *Enhanced Isolation and Release of Circulating Tumor Cells Using Nanoparticle Binding and Ligand Exchange in a Microfluidic Chip*. ACS Publications. https://pubs.acs.org/doi/pdf/10.1021/jacs.6b12236 (accessed 2021-12-31). https://doi.org/10.1021/jacs.6b12236.

(22) Cooke, T.; Reeves, J.; Lanigan, A.; Stanton, P. HER2 as a Prognostic and Predictive Marker for Breast Cancer. *Ann. Oncol.* **2001**, *12*, S23–S28. https://doi.org/10.1093/annonc/12.suppl_1.S23.

(23) Squires, T. M.; Messinger, R. J.; Manalis, S. R. Making It Stick: Convection, Reaction and Diffusion in Surface-Based Biosensors. *Nat. Biotechnol.* **2008**, *26* (4), 417–426. https://doi.org/10.1038/nbt1388.

(24) Pereiro, I.; Fomitcheva-Khartchenko, A.; Kaigala, G. V. Shake It or Shrink It: Mass Transport and Kinetics in Surface Bioassays Using Agitation and Microfluidics. *Anal. Chem.* **2020**. https://doi.org/10.1021/acs.analchem.0c01625.

(25) Hansen, R.; Bruus, H.; Callisen, T. H.; Hassager, O. Transient Convection, Diffusion, and Adsorption in Surface-Based Biosensors. *Langmuir* **2012**, *28* (19), 7557–7563. https://doi.org/10.1021/la3000763.

(26) Jin, D. S.; Brightbill, E. L.; Vogel, E. M. General Model for Mass Transport to Planar and Nanowire Biosensor Surfaces. *J. Appl. Phys.* **2019**, *125* (11), 114502. https://doi.org/10.1063/1.5084253.

(27) Schnell, U.; Cirulli, V.; Giepmans, B. N. G. EpCAM: Structure and Function in Health and Disease. *Biochim. Biophys. Acta BBA - Biomembr.* **2013**, *1828* (8), 1989–2001. https://doi.org/10.1016/j.bbamem.2013.04.018.

(28) Chen, L.; Peng, M.; Li, N.; Song, Q.; Yao, Y.; Xu, B.; Liu, H.; Ruan, P. Combined Use of EpCAM and FRα Enables the High-Efficiency Capture of Circulating Tumor Cells in Non-Small Cell Lung Cancer. *Sci. Rep.* **2018**, *8* (1), 1188. https://doi.org/10.1038/s41598-018-19391-1.

(29) Wit, S. de; Dalum, G. van; Lenferink, A. T. M.; Tibbe, A. G. J.; Hiltermann, T. J. N.; Groen, H. J. M.; van Rijn, C. J. M.; Terstappen, L. W. M. M. The Detection of EpCAM+ and EpCAM– Circulating Tumor Cells. *Sci. Rep.* **2015**, *5* (1), 12270. https://doi.org/10.1038/srep12270.

(30) Hatch, A.; Hansmann, G.; Murthy, S. K. Engineered Alginate Hydrogels for Effective Microfluidic Capture and Release of Endothelial Progenitor Cells from Whole Blood. *Langmuir* **2011**, *27* (7), 4257–4264. https://doi.org/10.1021/la105016a.

(31) Shah, A. M.; Yu, M.; Nakamura, Z.; Ciciliano, J.; Ulman, M.; Kotz, K.; Stott, S. L.; Maheswaran, S.; Haber, D. A.; Toner, M. Biopolymer System for Cell Recovery from Microfluidic Cell Capture Devices. *Anal. Chem.* **2012**, *84* (8), 3682–3688. https://doi.org/10.1021/ac300190j.

(32) Hye Myung, J.; A. Gajjar, K.; Eon Han, Y.; Hong, S. The Role of Polymers in Detection and Isolation of Circulating Tumor Cells. *Polym. Chem.* **2012**, *3* (9), 2336–2341. https://doi.org/10.1039/C2PY20420G.

(33) Perez-Gonzalez, V. H.; Gallo-Villanueva, R. C.; Camacho-Leon, S.; Gomez-Quiñones, J. I.; Rodriguez-Delgado, J. M.; Martinez-Chapa, S. O. Emerging Microfluidic Devices for Cancer Cells/Biomarkers Manipulation and Detection. *IET Nanobiotechnol.* **2016**, *10* (5), 263–275. https://doi.org/10.1049/iet-nbt.2015.0060.

(34) Antfolk, M.; Laurell, T. Continuous Flow Microfluidic Separation and Processing of Rare Cells and Bioparticles Found in Blood – A Review. *Anal. Chim. Acta* **2017**, *965*, 9–35. https://doi.org/10.1016/j.aca.2017.02.017.

(35) Zheng, S.; Lin, H. K.; Lu, B.; Williams, A.; Datar, R.; Cote, R. J.; Tai, Y.-C. 3D Microfilter Device for Viable Circulating Tumor Cell (CTC) Enrichment from Blood. *Biomed. Microdevices* **2011**, *13* (1), 203–213. https://doi.org/10.1007/s10544-010-9485-3.

(36) Coumans, F. A. W.; Dalum, G. van; Beck, M.; Terstappen, L. W. M. M. Filter Characteristics Influencing Circulating Tumor Cell Enrichment from Whole Blood. *PLOS ONE* **2013**, *8* (4), e61770. https://doi.org/10.1371/journal.pone.0061770.

(37) Tian, F.; Liu, C.; Lin, L.; Chen, Q.; Sun, J. Microfluidic Analysis of Circulating Tumor Cells and Tumor-Derived Extracellular Vesicles. *TrAC Trends Anal. Chem.* **2019**, *117*, 128–145. https://doi.org/10.1016/j.trac.2019.05.013.

(38) Cao, X.; Eisenthal, R.; Hubble, J. Detachment Strategies for Affinity-Adsorbed Cells. *Enzyme Microb. Technol.* **2002**, *31* (1), 153–160. https://doi.org/10.1016/S0141-0229(02)00083-2.

(39) Dhar, M.; Wong, J.; Che, J.; Matsumoto, M.; Grogan, T.; Elashoff, D.; Garon, E. B.; Goldman, J. W.; Sollier Christen, E.; Di Carlo, D.; Kulkarni, R. P. Evaluation of PD-L1 Expression on Vortex-Isolated Circulating Tumor Cells in Metastatic Lung Cancer. *Sci. Rep.* **2018**, *8* (1), 2592. https://doi.org/10.1038/s41598-018-19245-w.

(40) Kloten, V.; Lampignano, R.; Krahn, T.; Schlange, T. Circulating Tumor Cell PD-L1 Expression as Biomarker for Therapeutic Efficacy of Immune Checkpoint Inhibition in NSCLC. *Cells* **2019**, *8* (8), 809. https://doi.org/10.3390/cells8080809.

(41) Kulasinghe, A.; Perry, C.; Kenny, L.; Warkiani, M. E.; Nelson, C.; Punyadeera, C. PD-L1 Expressing Circulating Tumour Cells in Head and Neck Cancers. *BMC Cancer* **2017**, *17* (1), 333. https://doi.org/10.1186/s12885-017-3316-3.

(42) Janning, M.; Kobus, F.; Babayan, A.; Wikman, H.; Velthaus, J.-L.; Bergmann, S.; Schatz, S.; Falk, M.; Berger, L.-A.; Böttcher, L.-M.; Päsler, S.; Gorges, T. M.; O'Flaherty, L.; Hille, C.; Joosse, S. A.; Simon, R.; Tiemann, M.; Bokemeyer, C.; Reck, M.; Riethdorf, S.; Pantel, K.; Loges, S. Determination of PD-L1 Expression in Circulating Tumor Cells of NSCLC Patients and Correlation with Response to PD-1/PD-L1 Inhibitors. *Cancers* **2019**, *11* (6), 835. https://doi.org/10.3390/cancers11060835.

(43) Elster, N.; Collins, D. M.; Toomey, S.; Crown, J.; Eustace, A. J.; Hennessy, B. T. HER2-Family Signalling Mechanisms, Clinical Implications and Targeting in Breast Cancer. *Breast Cancer Res. Treat.* **2015**, *149* (1), 5–15. https://doi.org/10.1007/s10549-014-3250-x.

(44) Oh, D.-Y.; Bang, Y.-J. HER2-Targeted Therapies — a Role beyond Breast Cancer. *Nat. Rev. Clin. Oncol.* **2020**, *17* (1), 33–48. https://doi.org/10.1038/s41571-019-0268-3.

(45) Ahn, S.; Woo, J. W.; Lee, K.; Park, S. Y. HER2 Status in Breast Cancer: Changes in Guidelines and Complicating Factors for Interpretation. *J. Pathol. Transl. Med.* **2020**, *54* (1), 34–44. https://doi.org/10.4132/jptm.2019.11.03.

(46) Wülfing, P.; Borchard, J.; Buerger, H.; Heidl, S.; Zänker, K. S.; Kiesel, L.; Brandt, B. HER2-Positive Circulating Tumor Cells Indicate Poor Clinical Outcome in Stage I to III Breast Cancer Patients. *Clin. Cancer Res.* **2006**, *12* (6), 1715–1720. https://doi.org/10.1158/1078-0432.CCR-05-2087.

(47) Huang, T.; Jia, C.-P.; Jun-Yang; Sun, W.-J.; Wang, W.-T.; Zhang, H.-L.; Cong, H.; Jing, F.-X.; Mao, H.-J.; Jin, Q.-H.; Zhang, Z.; Chen, Y.-J.; Li, G.; Mao, G.-X.; Zhao, J.-L. Highly Sensitive Enumeration of Circulating Tumor Cells in Lung Cancer Patients Using a Size-Based Filtration Microfluidic Chip. *Biosens. Bioelectron.* **2014**, *51*, 213–218. https://doi.org/10.1016/j.bios.2013.07.044.

(48) Allard, W. J.; Matera, J.; Miller, M. C.; Repollet, M.; Connelly, M. C.; Rao, C.; Tibbe, A. G. J.; Uhr, J. W.; Terstappen, L. W. M. M. Tumor Cells Circulate in the Peripheral Blood of All Major Carcinomas but Not in Healthy Subjects or Patients With Nonmalignant Diseases. *Clin. Cancer Res.* **2004**, *10* (20), 6897–6904. https://doi.org/10.1158/1078-0432.CCR-04-0378.

(49) Chen, J.-F.; Ho, H.; Lichterman, J.; Lu, Y.-T.; Zhang, Y.; Garcia, M. A.; Chen, S.-F.; Liang, A.-J.; Hodara, E.; Zhau, H. E.; Hou, S.; Ahmed, R. S.; Luthringer, D. J.; Huang, J.; Li, K.-C.; Chung, L. W. K.; Ke, Z.; Tseng, H.-R.; Posadas, E. M. Subclassification of Prostate Cancer Circulating Tumor Cells by Nuclear Size Reveals Very Small Nuclear Circulating Tumor Cells in Patients with Visceral Metastases. *Cancer* **2015**, *121* (18), 3240–3251. https://doi.org/10.1002/cncr.29455.

(50) Myung, J. H.; Eblan, M. J.; Caster, J. M.; Park, S.-J.; Poellmann, M. J.; Wang, K.; Tam, K. A.; Miller, S. M.; Shen, C.; Chen, R. C.; Zhang, T.; Tepper, J. E.; Chera, B. S.; Wang, A. Z.; Hong, S. Multivalent Binding and Biomimetic Cell Rolling Improves the Sensitivity and Specificity of Circulating Tumor Cell Capture. *Clin. Cancer Res.* **2018**, *24* (11), 2539–2547. https://doi.org/10.1158/1078-0432.CCR-17-3078.

(51) Zhang, P.; Zhou, X.; He, M.; Shang, Y.; Tetlow, A. L.; Godwin, A. K.; Zeng, Y. Ultrasensitive Detection of Circulating Exosomes with a 3D-Nanopatterned Microfluidic Chip. *Nat. Biomed. Eng.* **2019**, *3* (6), 438–451. https://doi.org/10.1038/s41551-019-0356-9.

(52) Kuske, A.; Gorges, T. M.; Tennstedt, P.; Tiebel, A.-K.; Pompe, R.; Preißer, F.; Prues, S.; Mazel, M.; Markou, A.; Lianidou, E.; Peine, S.; Alix-Panabières, C.; Riethdorf, S.; Beyer, B.; Schlomm, T.; Pantel, K. Improved Detection of Circulating Tumor Cells in Non-Metastatic High-Risk Prostate Cancer Patients. *Sci. Rep.* **2016**, *6* (1), 39736. https://doi.org/10.1038/srep39736.

(53) Zhang, Y.; Giacchetti, S.; Parouchev, A.; Hadadi, E.; Li, X.; Dallmann, R.; Xandri-Monje, H.; Portier, L.; Adam, R.; Lévi, F.; Dulong, S.; Chang, Y. Dosing Time Dependent in Vitro Pharmacodynamics of Everolimus despite a Defective Circadian Clock. *Cell Cycle* **2018**, *17* (1), 33–42. https://doi.org/10.1080/15384101.2017.1387695.

(54) *Transport and Adsorption*. COMSOL. https://www.comsol.com/model/transport-and-adsorption-5 (accessed 2021-12-31).

Flow Rate Independent Multiscale Liquid Biopsy for Precision Oncology

Supplementary Material

Jing Yan[1], Jie Wang[2], Robert Dallmann[3], Renquan Lu[4], and Jérôme Charmet*[3,5]*

1 Holosensor Medical Technology Ltd. Suzhou, 215000, China,
2. Institute for Advanced Materials, School of Material Science and Engineering, Jiangsu University, Zhenjiang 212013, China,
3 Division of Biomedical Sciences, Warwick Medical School, University of Warwick, Coventry CV4 7AL, United Kingdom,
4 Department of Clinical Laboratory, Fudan University Shanghai Cancer Center, Shanghai, 200032, China,
5 School of Engineering – HE-Arc Ingénierie, HES-SO University of Applied Sciences Western Switzerland, 2000 Neuchâtel, Switzerland.

Flow rate independence and conventional microfluidics.

In conventional microfluidic devices, the effective cross-section *A* is constrained by the micron length scale in one dimension and by the microfabrication processes (e.g. aspect ratio) or practical considerations (structural stability, etc.) in the other. In other words, the flow rate *Q* and the fluid velocity *v* are coupled through the square of the length scale, as given by $v \propto Q/L^2$. Therefore, any attempt to reduce the fluid velocity results in a lower interaction probability. Indeed, given a flow rate *Q*, the fluid velocity *v* can be decreased through an increase of the channel in cross-section A (as given by *v=Q/A*). However, this increases the length scale *L* (since $A \propto L^2$), which in turn decreases the interaction probability between cells and surface.

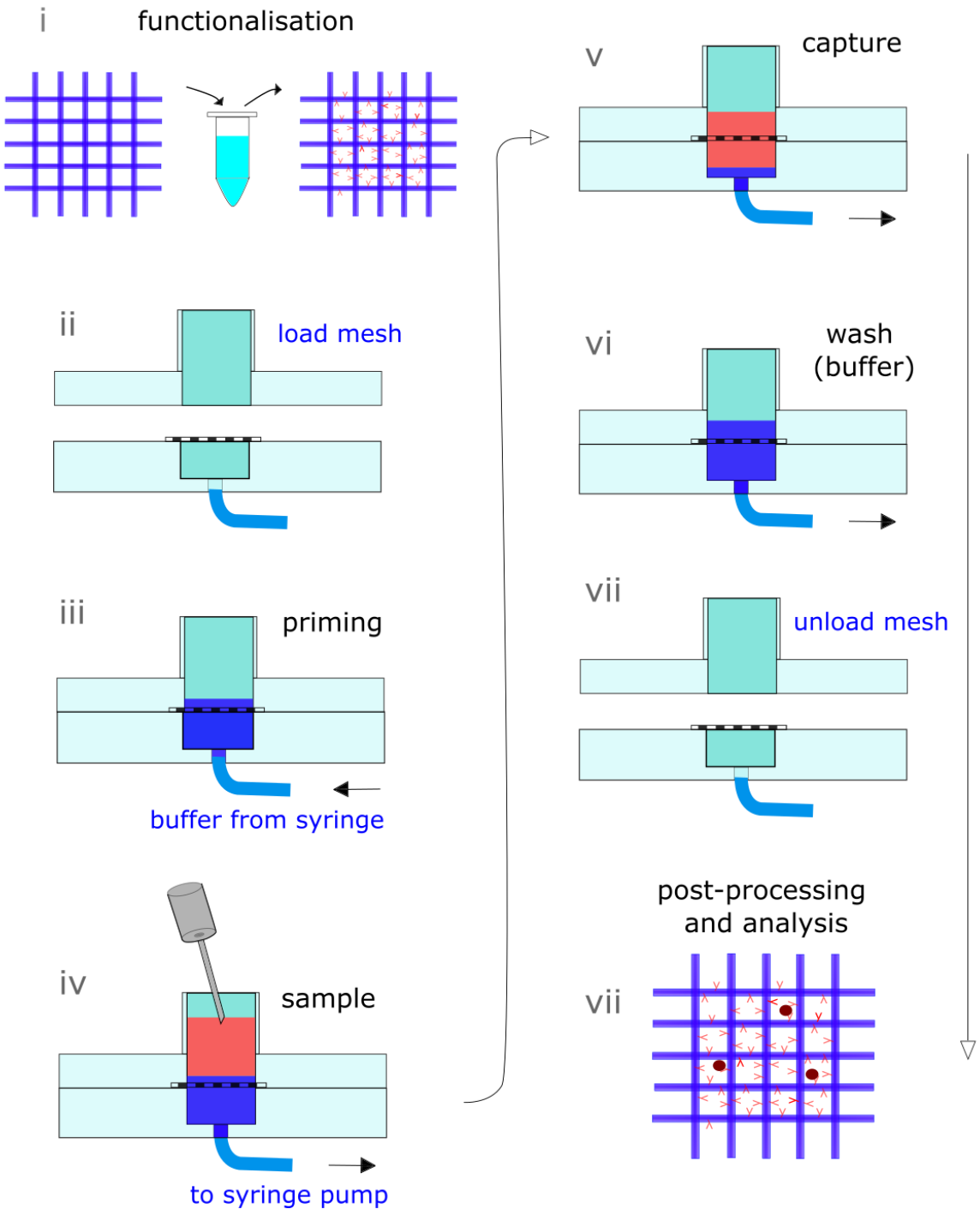

Figure SM1. Schematic of process steps from pre-processing (functionalisation) to post-processing (e.g., fluorescence microscopy).

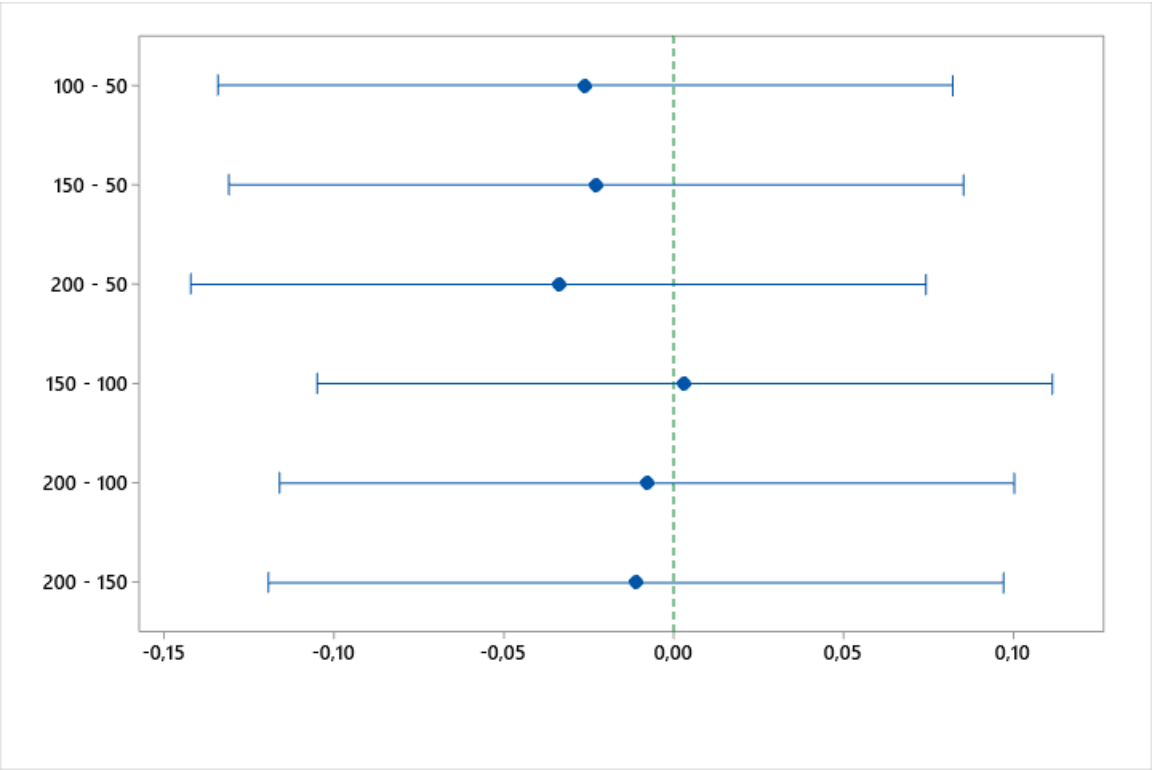

Figure SM2. Graphs showing the post-hoc Tukey's test on flow rate independent data (Fig 2a). Each set (flow rate in µL min^{-1}) includes zero, which means that there is no statistical difference between any of the sets.

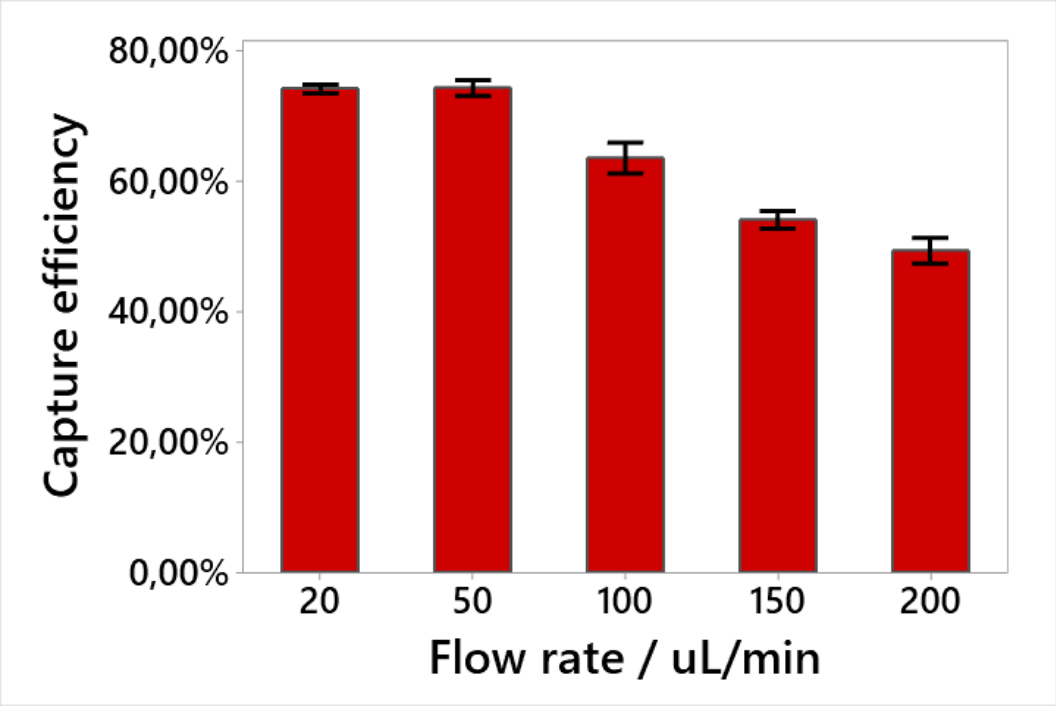

Figure SM3. Graph showing the flow rate dependence of the device with a fixed diameter (6 mm in this case). An extra flow rate (20 µL min^{-1}) was added here to show the drop-off point at 50 µL min^{-1}, compared to Fig. 2.

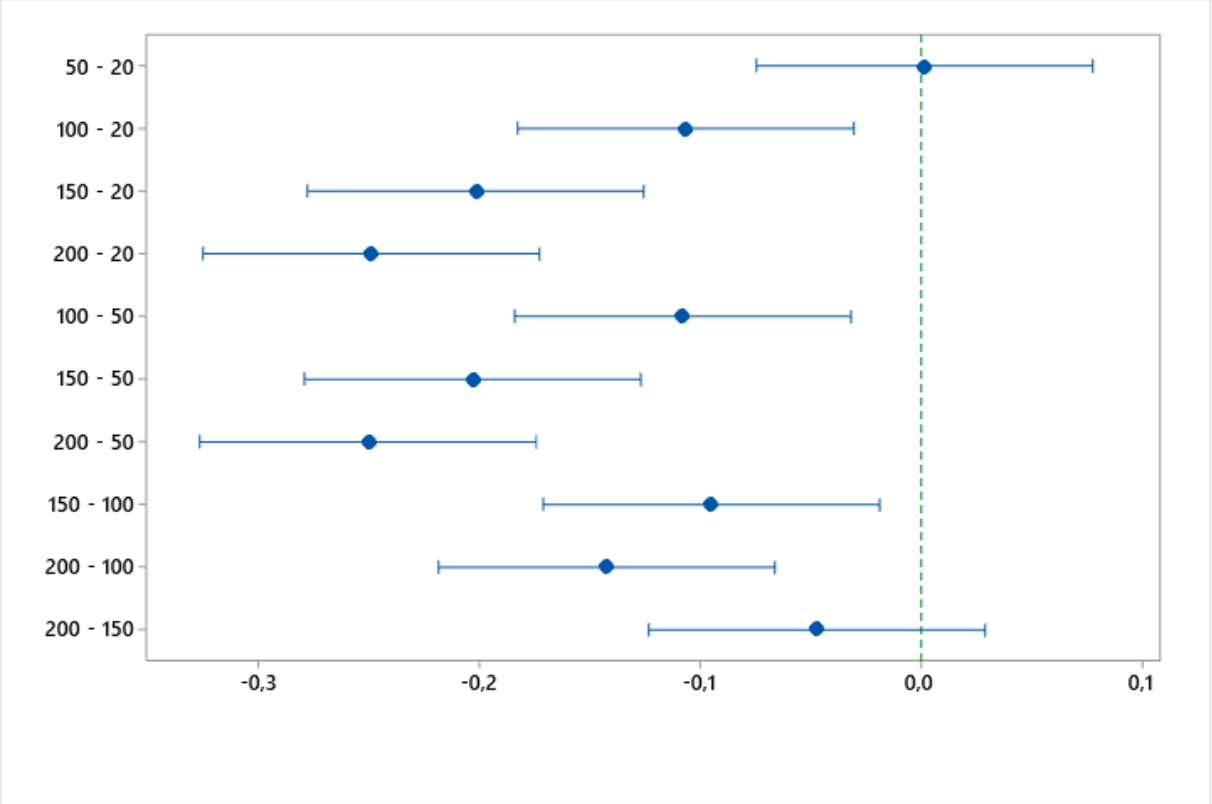

Figure SM4. Graphs showing the post-hoc Tukey's test on flow rate dependent data (Fig SM3 above). Two sets (20 – 50 µL min^{-1} and 200 – 150 µL min^{-1}) include zero, which means that there is no statistical difference between any of the sets. The rest of the sets are significantly different, confirming flow rate dependence on the capture efficiency.

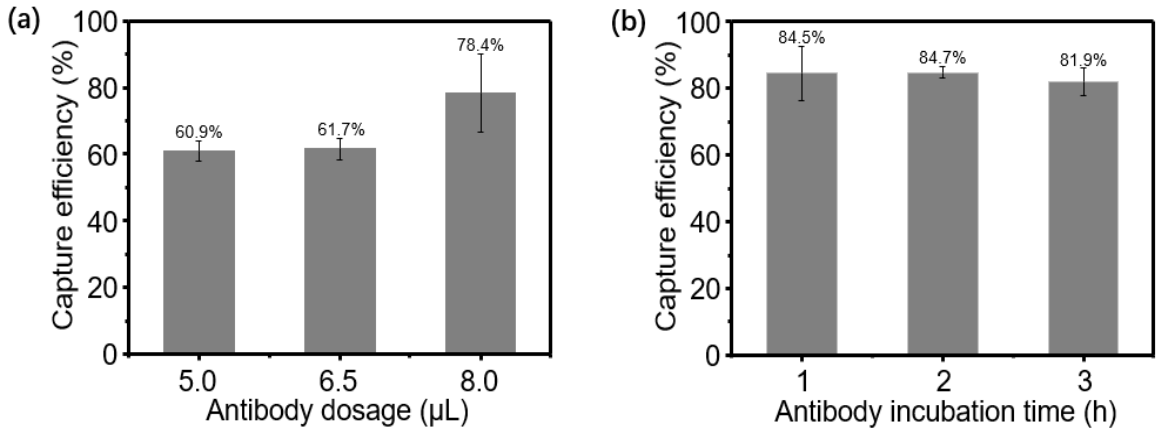

Figure SM5. Antibody optimisation against capture efficiency (MCF-7 cells). The capture efficiency increases significantly for an 8 µL antibody dose compared 6.5 µL and 5 µL (a). This value was chosen for further analyses. Different incubation times between the polymer and anti-EpCAM antibodies were tested (b). No significant differences were observed for incubation times between 1h to 3h. The capture efficiency increases significantly for an 8 µL antibody dose compared 6.5 µL and 5 µL (a). This value was chosen for further analyses. Different incubation times between the polymer and anti-EpCAM antibodies were tested (b). No significant differences were observed for incubation times between 1h to 3h.

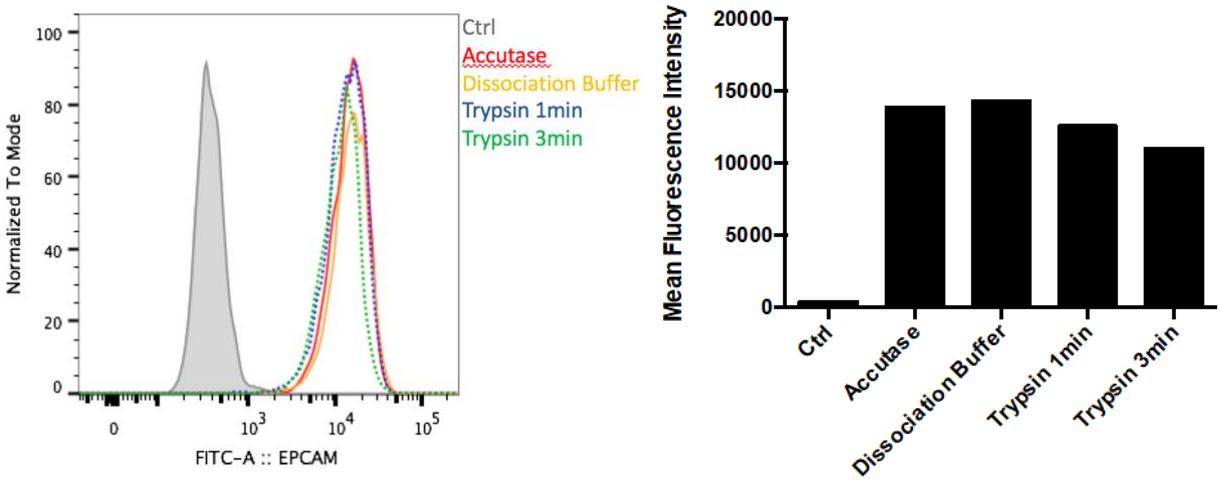

Figure SM6. Control and optimisation of harvesting parameters and antibody selection. MCF-7 cells were stained with FITC anti-EPCAM (Clone: 9C4, Biolegend) and their EPCAM expression level was evaluated using flow cytometry. Other antibodies were tested but did not produce better results – not shown. Different harvesting reagents and parameters were tested to evaluate their effect on EpCAM expression. The effects of cell dissociation buffer in PBS, Accutase, 0.25% Trypsin (1 and 3 minutes) under standard conditions were characterised. Our results show that cell dissociation buffer in PBS or Accutase provide a gentler process, maintaining EpCAM integrity.

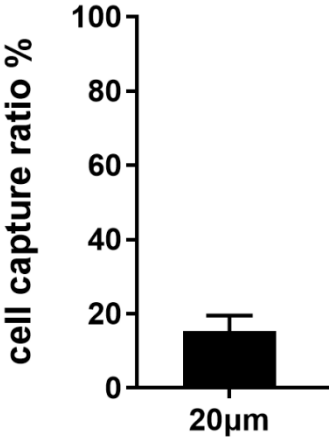

Figure SM7. Traut reagent was used as a functionalisation strategy to tether the anti-EpCAM antibodies onto the gold coated mesh. However, the capture efficiency, presented here for a 20 x 20 µm pore size in a 6 mm diameter mesh at 50 µL min^{-1}, shows less than 20% capture efficiency, compared to over 60% in the same conditions with our HA-SH nanobranched polymer (Fig. 4C).

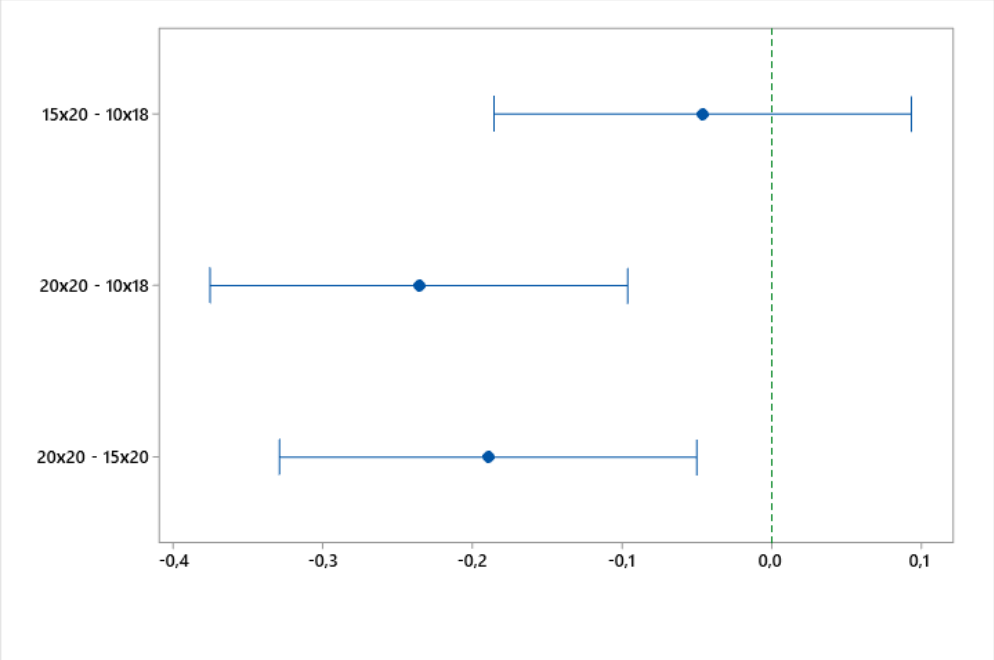

Figure SM8. Graphs showing the post-hoc Tukey's test on the capture efficiency as a function of pore sizes. Figure 4c shows that the capture efficiency increases with decreasing pore sizes, however the graph above shows that the set (10x18 – 15x20 µm) includes zero, which means that there is no statistical difference between the two sets.

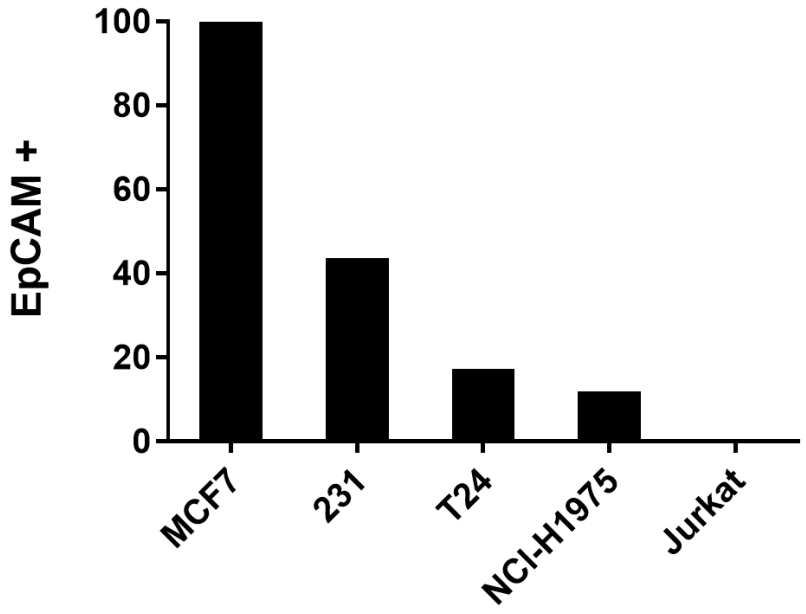

Figure SM9. We compared the capture efficiency of MCF-7 cells with MDA-MB-231, T24, NCl-H1975 and Jurkat cells in Figure 4e. Here, we show that the relative capture efficiencies are in agreement with the EpCAM expression level of each cell type, as measured using flow cytometry. The data of each cell type is relative to the EpCAM expression level of MCF7, which is set to 100%. The results are in line with data from the gene expression atlas (Gene ID ENSG00000119888).

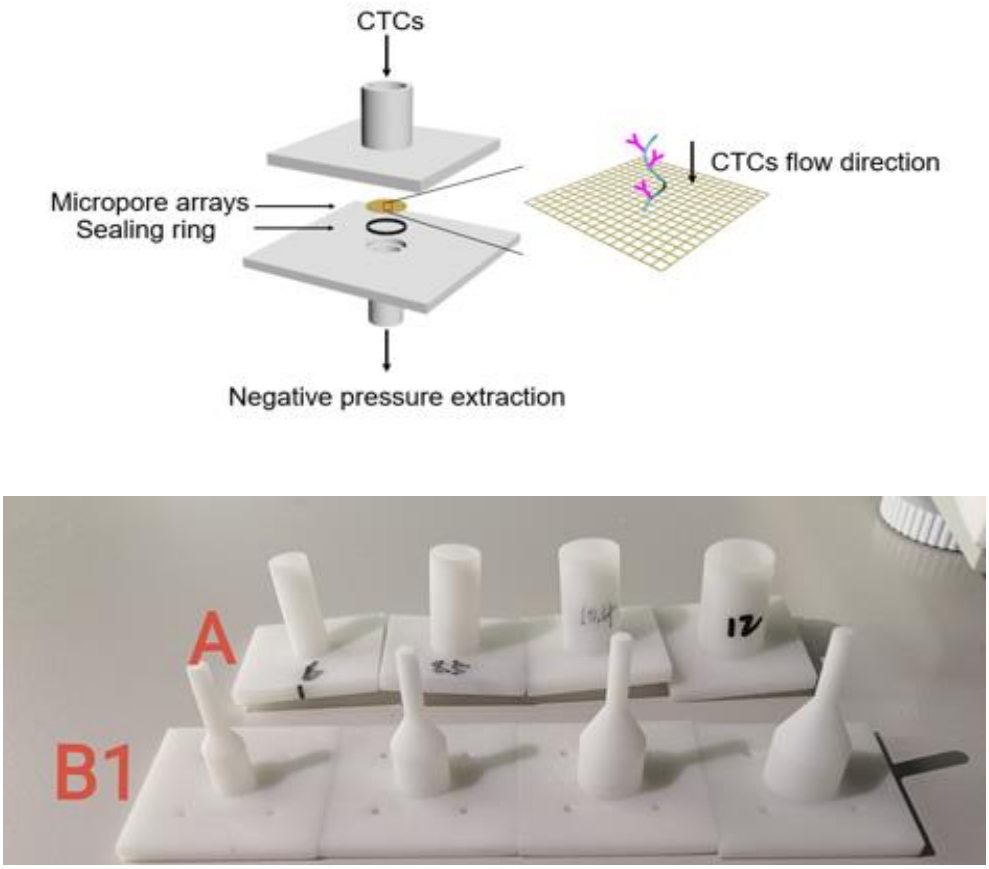

Figure SM10. Device architecture and mesh holder. A schematic representing the assembly of the mesh in the holder (top) and different mesh holders used to evaluate the flow rate independence are shown (bottom).

Table S1 (a): Details of patients enrolled in the first and second studies and raw results for CTCs and PD-L1+ CTCs counts.

Sample	Gender	Age	Date	Diagnosis	Detection type	Number		Rate
						CTC	CTC PD-L1	
1	F	61	2019.07.29	NSCLC	CTC+ PD-L1	5	2	40.0%
2	M	53	2019.08.01	NSCLC	CTC+ PD-L1	3	1	33.3%
3	F	60	2019.08.01	NSCLC	CTC+ PD-L1	2	0	0.0%
4	M	51	2019.08.04	NSCLC	CTC+ PD-L1	5	0	0.0%
5	M	84	2019.08.25	NSCLC	CTC+ PD-L1	7	0	0.0%
6	F	49	2019.09.03	NSCLC	CTC+ PD-L1	2	0	0.0%
7	M	46	2019.09.05	NSCLC	CTC+ PD-L1	6	2	33.3%
8	F	58	2019.11.24	NSCLC	CTC+ PD-L1	6	0	0.0%
9	M		2019.11.25	NSCLC	CTC+ PD-L1	4	0	0.0%
10	M		2019.11.28	NSCLC	CTC+ PD-L1	4	0	0.0%
11	F	47	2019.12.09	NSCLC	CTC+ PD-L1	2	1	50.0%
12	M	68	2019.12.26	NSCLC	CTC+ PD-L1	4	1	25.0%
13	M		2019.12.27	NSCLC	CTC+ PD-L1	2	1	50.0%
14	M		2019.12.28	NSCLC	CTC+ PD-L1	2	1	50.0%
15	F		2019.12.28	NSCLC	CTC+ PD-L1	9	1	11.1%
16	F		2020.01.10	NSCLC	CTC+ PD-L1	3	1	33.3%
17	M		2020.01.10	NSCLC	CTC+ PD-L1	2	0	0.0%
18	M		2020.01.10	NSCLC	CTC+ PD-L1	3	0	0.0%
19	M		2020.03.16	NSCLC	CTC+ PD-L1	6	0	0.0%
20			2020.03.23	NSCLC	CTC+ PD-L1	4	0	0.0%
21	M	56	2020.04.17	colorectal cancer	CTC+ PD-L1	3	0	0.0%
22	F	62	2020.04.17	colorectal cancer	CTC+ PD-L1	3	2	66.7%
23	F	64	2020.05.09	colorectal cancer	CTC+ PD-L1	4	0	0.0%
24	F		2020.05.26	NSCLC	CTC+ PD-L1	5	4	80.0%
25	M	57	2020.06.05	SCLC	CTC+ PD-L1	3	2	66.7%
26			2020.06.05	liver cancer	CTC+ PD-L1	6	0	0.0%
27	M	51	2020.06.14	Pulmonary nodules	CTC+ PD-L1	3	0	0.0%
28			2020.06.05	liver cancer	CTC+ PD-L1	2	0	0.00%
29			2020.06.05	liver cancer	CTC+ PD-L1	6	0	0.00%
30			2020.06.30	liver cancer	CTC+ PD-L1	2	0	0.00%
31	F	76	2022.01.14	liver cancer	CTC+ PD-L1	1	0	0.00%
32	M	36	2022.02.15	liver cancer	CTC+ PD-L1	1	0	0.00%
33	F	74	2022.02.10	pancreatic carcinoma	CTC+ PD-L1	0	0	0.00%

Table S1 (b): Details of patients enrolled in the first study and raw results for CTCs counts only (ctd) and healthy volunteers (below).

Sample	Gender	Age	Date	Diagnosis	Detection type	CTC number
1	M		2019.08.23	NSCLC	CTC	6
2	M		2019.08.23	NSCLC	CTC	4
3	M		2019.08.27	NSCLC	CTC	1
4	M		2019.08.27	NSCLC	CTC	3
5	M		2019.08.27	NSCLC	CTC	2
6	M		2019.08.27	NSCLC	CTC	1
7	M		2019.08.27	NSCLC	CTC	5
8	M		2019.08.30	NSCLC	CTC	4
9	F		2019.08.30	NSCLC	CTC	4
10	M		2019.08.30	NSCLC	CTC	2
11	M		2019.08.30	NSCLC	CTC	4
12	F		2019.09.13	NSCLC	CTC	5
13	M		2019.10.26	NSCLC	CTC	2
14	M	42	2019.12.24	nasopharynx cancer	CTC	14
15	F		2020.03.14	cancer of biliary duct	CTC	3
16			2020.06.30	liver cancer	CTC	2
17	F	40	2019.11.21	breast cancer	CTC	4
18	F	51	2020.01.02	breast cancer	CTC	5
19	F	68	2020.03.12	breast cancer	CTC	2
20	F	66	2020.03.12	breast cancer	CTC	2

Number	Sampling time	Age	Gender	CTC
1	2021.12.04	29	Male	0
2	2021.12.04	28	Male	0
3	2021.12.04	31	Female	0
4	2021.11.25	24	Male	0
5	2021.11.25	29	Male	0
6	2021.11.25	35	Male	0
7	2021.11.26	24	Female	0
8	2021.11.26	28	Female	0
9	2021.11.26	29	Male	0
10	2021.12.28	31	Female	0
11	2021.12.28	31	Male	0
12	2021.12.28	30	Male	0
13	2021.12.28	33	Male	0
14	2021.12.28	32	Male	0
15	2021.12.19	28	Male	0
16	2021.12.19	26	Male	0
17	2021.12.19	29	Female	0
18	2021.12.19	24	Female	0
19	2021.12.20	27	Male	0
20	2021.12.20	27	Male	0

Table S2: Details of patients enrolled in the first and third study and raw results for CTCs counts and HER2+ CTCs.

Time	NO.	Age	Diagnosis				Tissue grade	T	N	M	TNM	IHC HER2	FISH HER-2	ER	PR	Size	CTC	HER-2 CTC
2020.09.24	**1**	74	Breast cancer	Malignant	Invasive	Ductal carcinoma	3	2	1	0	ⅡB	2+	(-)	80%，+	60%，+	1.3*1.3*1 cm	2	0
2020.11.06	**2**	41	Breast cancer	Malignant	Invasive	Ductal carcinoma	2	0	0	0	0	2+	(-)	95%，+	60%，+	/	1	0
2020.11.06	**3**	77	Breast cancer	Malignant	Invasive	Ductal carcinoma	3	2	0	0	ⅡA	2+	(-)	80%，+	80%，+	2*1.8*1.5 cm	1	0
2020.11.13	**4**	48	Breast cancer	Malignant	Invasive	Ductal carcinoma	3	2	0	0	ⅡA	3+	(+)	-	-	4*3.5*2c m	5	2
2020.11.13	**5**	60	Breast cancer	Malignant	Invasive	Ductal carcinoma	2	3	1	0	ⅢA	2+	(+)	-	-	5×4×2cm	11	6
2020.11.13	**6**	71	Breast cancer	Malignant	Invasive	Apocrine sweat gland carcinoma	2	1	0	0	Ⅰ	2+	(-)	-	-	1.2*0.9*0 .8cm	8	6
2020.11.17	**7**	59	Breast cancer	Malignant	/	/	/	/	/	/	/	2+	(-)	90%，+	80%，+	/	5	0
2020.12.02	**8**	33	Breast cancer	Malignant	Invasive	Ductal carcinoma	2	/	/	/	/	2+	(-)	80%，+	90%，+	2.5×1.5×1 .5cm	10	6
2020.12.02	**9**	63	Breast cancer	Malignant	Invasive	Ductal carcinoma	2	1	0	0	Ⅰ	2+	(+)	80%，+	1%	2×1×1cm	8	5
2020.12.03	**10**	41	Breast cancer	Malignant	Invasive	Ductal carcinoma	2	3	0	0	ⅡB	2+	(-)	80%，+	80%，+	6×3×2cm	5	0
2020.12.03	**11**	42	Breast cancer	Malignant	Invasive	Ductal carcinoma	2	/	/	/	/	2+	(-)	70%，+	70%，+	1.6×1.1×1 .3cm	5	1

Time	NO.	Age	Diagnosis				Tissue grade	T	N	M	TNM	IHC HER2	FISH HER-2	ER	PR	Size	CTC	HER-2 CTC
2020.12.07	**12**	56	Breast cancer	Malignant	Invasive	Ductal carcinoma	3	/	/	/	/	2+	(-)	-	-	2×1.5×1cm	2	1
2020.12.08	**13**	31	Breast cancer	Malignant	Invasive	Ductal carcinoma	3	/	/	/	/	2+	(+)	90%，+	80%，+	/	7	1
2020.12.09	**14**	27	Breast cancer	Malignant	/	/	/	2	2	1	Ⅳ	2+	(+)	-	-	/	0	0
2020.12.10	**15**	49	Breast cancer	Malignant	/	/	/	/	/	/	/	3+	(+)	70%，+	2%，	25×25×15 mm	3	0
2020.12.11	**16**	36	Breast cancer	Malignant	Invasive	Ductal carcinoma	3	1	1	0	ⅡA	2+	(-)	-	-	1.1×1×0.9 cm	1	1
2020.12.11	**17**	48	Breast cancer	Malignant	Invasive	Ductal carcinoma	2	1	0	0	Ⅰ	2+	(-)	80%，+	80%，+	1.5×1×1 cm	5	0
2020.12.14	**18**	41	Breast cancer	Malignant	Invasive	Ductal carcinoma	2--3	2	1	0	ⅡB	2+	(+)	80%，+	80%，+	2.5×1.5×1.3 cm	5	0
2020.12.14	**19**	68	Breast cancer	Malignant	Invasive	Ductal carcinoma	3	/	/	/	/	2+	(+)	-	-	1.4×1.2×1 cm	5	1
2020.12.15	**20**	56	Breast cancer	Malignant	Invasive	Ductal carcinoma	2	1	0	0	Ⅰ	2+	(-)	60%，+	1%，+	2×1.2×1.1 cm	7	1
2020.12.15	**21**	65	Breast cancer	Malignant	Invasive	Ductal carcinoma	3	2	1	0	ⅡB	2+	(+)	90%，+	2%	2×2×2 cm	2	1
2020.12.16	**22**	36	Breast cancer	Malignant	Invasive	/	/	/	/	/	/	1+	(-)	10%	-	/	7	0
2020.12.21	**23**	47	Breast cancer	Malignant	Invasive	Ductal carcinoma	2	x	0	0		2+	(-)	80%，+	80%，+	/	0	0

Time	NO.	Age	Diagnosis				Tissue grade	T	N	M	TNM	IHC HER2	FISH HER-2	ER	PR	Size	CTC	HER-2 CTC
2020.12.22	**24**	49	Breast cancer	Malignant	Invasive	Ductal carcinoma	3	/	/	/	/	3+	(+)	-	-	2*2*1cm	7	1
2020.12.24	**25**	50	Breast cancer	Malignant	Invasive	/	2	/	/	/	/	2+	(-)	90%，+	90%，+	2×2×1cm	3	0
2020.12.28	**26**	43	Breast cancer	Malignant	Invasive	Lobular carcinoma	2	1	1	0	ⅡA	1+	(-)	80%，+	80%，+	2.5×2×1.5 cm	1	1